To the best girlfriend ever, to the only one in the world that deserve my love, and to the one that i will love until the end of Time.

Introduction

Ring laser "gyros" are nowadays standard sensors in high sensitivity inertial guidance, angle metrology, and more generally in estimating rotation rates. They combine unique qualities of stability with reference to the measure operation, high sensitivity, wide frequency detection range, absence of moving mechanical part, lack of sensitivity to linear accelerations, reliability and duration.

As discovered by G. Sagnac (1913), using pure classical formalism [1], interference pattern of two light beams following the same closed path in opposite directions is proportional to the rotation rate of the closed path. Sensitivity to rotation is the fundamental feature of the Ring Laser Gyroscopes (RLG) and, together with the above mentioned properties, make this instrument of great interest in military and civil applications [2]. Many improvements in the RLG design and implementation have been achieved in the last decades [2].

Recent manufacturing progresses together with new statistical tools for data treatment allow one to further investigate extremely various field of application, such as very accurate motion sensing ($\sim 10^{-2}$ deg/h), servo navigation control, Geophysics, Geodesy and General Relativity.

Aim of this thesis is to provide a statistical tool for the identification of RLG parameters and the subsequent estimate of the rotation rate, focusing on the improving of sensitivity and long term stability, for instance the minimization of the Allan variance of rotational noise over long timescales [3]).

The plan of the thesis is as follows. In Section 1 the Sagnac effect is explained and its basic static model is presented. In Section 2 an overview of the RLG manufacturing techniques is given, with attention to G-PISA experiment [4], to which this work is devoted. A full model of the RLG dynamic which accounts for non-reciprocity in propagating beams, as well as noise presence and control loops, is afforded in Section 3. Section 4 describes an identification procedure designed for G-PISA. Section 5 is devoted to Extended Kalman

Filter (EKF [5]) routine that we devised for the estimate of the low frequency rotation rate of G-PISA. Finally, in Section 6 we presents our results and conclusions about the use of EKF for the rotation estimation.

Contents

1 Sagnac Effect

Sagnac effect was not fully understood even by Sagnac itself, who described it as a proof of the existence of the "ether", in opposition to the Theory of Relativity. Einstein and many other physicists have substantially improved the description of the effect, so that the Sagnac effect is considered now to be a relativistic effect[1]. As an example of their investigations, we can mention the question whether it is possible or not to measure an absolute rotation rate by an experiment conducted entirely within a rotating frame. Actually, the rotation rate is considered a time-reversal violating parameter, and issues of modern physics ranging from quantum theory on fundamental symmetries testing to General Relativity, still arises. The experimentation of high sensitivity RLG is therefore expected to open new windows on some of these issues [6].

Sagnac effect has been discovered for the first time with the use of passive ring interferometer. In such devices light enters the setup from outside, and it is divided at a beam splitter. The two beams are made to follow the same trajectory in opposite directions and recombined. The position of the interference fringes depend on the angular velocity of the apparatus.

One can instead consider a ring interferometer that is self-contained, exploiting laser technology: the light is generated and sustained by incorporating laser excitation in the path of the light, the resulting device is called 'ring laser', and what is measured is frequency shift. Active (laser) interferometry is usually preferred to passive one for several reasons as absolute calibration and robustness. In fact, light must be split and recombined in the passive device, while laser autonomously seek the resonance modes of the optical cavity which the laser is coupled to.

Both interferometers working scheme are sketched in Fig.1.1

In this work we will deal with active interferometers and it is useful to provide in the following a simple explanation of their working principle [7].

In order to make laser oscillation possible one must require that:

i) *Laser Threshold Condition* The cavity losses are balanced by oscillator gain at the frequency of oscillation

ii) *Laser Resonance Condition* There is an integer number of light wavelengths in the cavity path of both laser radiation, i.e. $n\lambda = L_\pm$
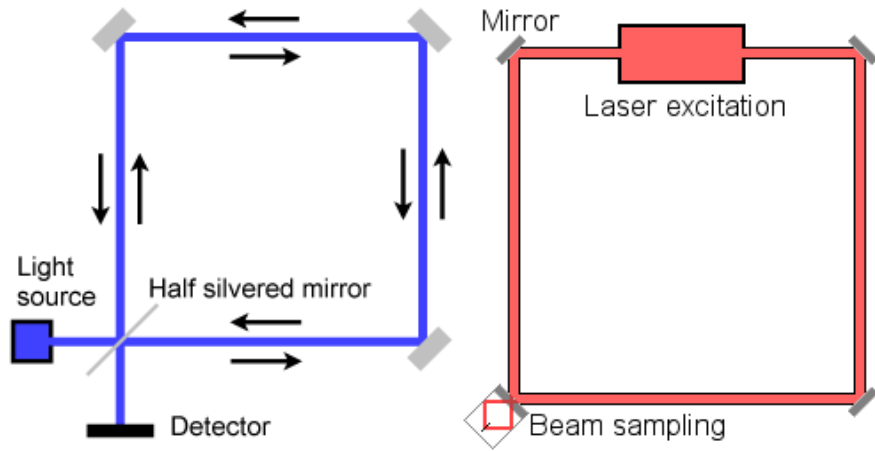
Figure 1.1: Schematic representations of a Sagnac interferometer (Left Figure), and of a ring laser setup (Right Figure).
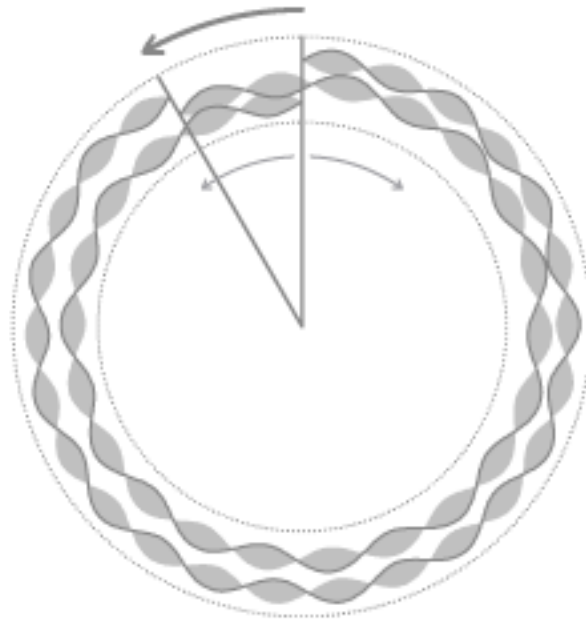

Figure 1.2: Schematic representation of the frequency shift when a ring laser interferometer is rotating. Both the counter propagating light and the co-propagating light go through 12 cycles of their frequency.

where n is an integer, $L_\pm$ is the optical path of the beam in the cavity referred to the co-rotating and counter-rotating waves, and λ is the wavelength of the laser in the medium that fills the cavity. See Fig. 1.2.

We introduce the notation $'\pm'$ for the two waves direction: we will use the label $'+'$ for the wave propagating clockwise, and $'-'$ for the counter-clockwise one respectively. Rewriting the above relation in terms of beam frequencies $\nu_\pm$, one obtain $\nu_\pm = n\,c\,/\,L_\pm$, being c the speed of light. Thus, differentiating

$$\frac{\delta\nu}{\nu} = \frac{\delta L}{L} \qquad , \tag{1.1}$$

where $\delta\nu$ and δL are the variations around the nominal value (averaged) of $\pm$ cases. The rotation, i.e. the change in path length for the oscillating beams, can be monitored by the frequency difference between the two propagating waves.

To better clarify what happens, consider a circular non rotating cavity referred to an inertial frame: each beam follows a path of almost the same length if the cavity symmetry condition holds, thus the two paths are covered by light in same time. If the cavity counter-clockwise rotates with respect to the inertial frame, as the speed of light is independent of the reference frame, the transit times $t_\pm$ of the two waves will be different and the beam co-rotating with the cavity will arrive before than the counter-rotating one, i.e.

$$t_+ = \frac{2\pi R}{(c - R\Omega)} \qquad t_- = \frac{2\pi R}{(c + R\Omega)} \qquad , \tag{1.2}$$

where R is the radius of the cavity, and Ω its rotation rate. The time difference reads

$$\Delta t = \frac{4A\Omega}{c^2} \qquad , \tag{1.3}$$

where A is the area enclosed by the two paths. It is worth noticing that Eq. (1.3) still holds with any other close planar path geometry [17]. So, by multiplying the relation given by c we get

$$\Delta L = \frac{4A\Omega}{c} \qquad . \tag{1.4}$$

The factors c^2 and c at denominator of Eqs. (1.2) and (1.4) make infeasible any direct measure of the differential transit time or path length, as they are usually of the order of 10^{-20} s and 10^{-12} m [17]. The measured quantity is rather the frequency difference, respectively

$$\Delta\nu = \frac{4A\Omega}{\lambda L} \quad .$$ (1.5)

For a typical RLG with $4\,m$ perimeter and $1\,m^2$ area, filled with helium-neon [17] so that $\lambda = 0.663\,\mu m$, $\Delta\nu = 3.04 \cdot (\Omega \cdot 10/2\pi)\,[deg/h]\,Hz$, for rotation rates closes to the earth one ($\Omega = 360/24\,deg/h$), the frequency shift is $45.7\,Hz$, which turns out to be easily measurable.

Eq. (1.5) states the main feature of high sensitivity RLG: to detect rotation rates with good accuracy rings must have a large size, modern high sensitivity RLG exceed one meter of side. Its worth noticing that a larger device will result in more stringent constraints on components manufacture and in bigger noise dynamics, thus the frequency estimating routine based on Kalman filter represent a crucial component of these devices.

To provide an index of the RLG sensitivity, consider the integrated version of Eqs. (1.5)

$$N = \frac{4A}{\lambda L} \cdot \Theta \quad ,$$ (1.6)

where N is the number of cycles of the beat frequency, and Θ the rotation angle. The angle the RLG should be rotated to obtain an unit increase of N is taken as scale factor

$$SF = \frac{\lambda L}{4A} \quad .$$ (1.7)

Empirically N is measured for a full revolution (i.e. $\Theta = 2\pi$), and hence the scale factor described is determined as:

$$SF = \frac{2\pi}{N}.$$ (1.8)

For typical RLG parameters $SF \sim 0.01\,arcsec/count$.

However, this model is not sufficiently accurate to describe the dynamics of a RLG, due to the non-idealities of a practical realization of the experiment, e.g.

Figure 1.3: The two operational configurations of the experimental setup of G-PISA.
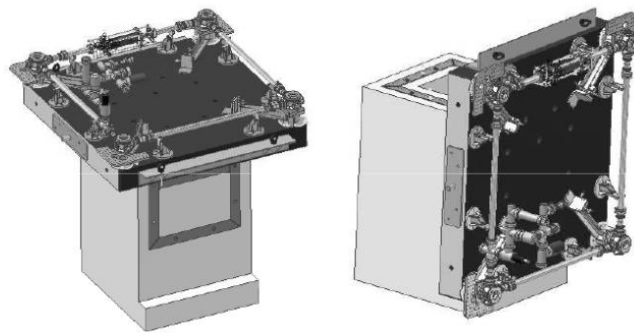

Figure 1.4: Mechanical design of G-PISA gyroscope in the two possible orientations of the laser plane.

non-linear behavior and parameters variation. To deal with such complex non-linear devices, a description of the RLG called G-PISA is given, and a more detailed and useful model of the apparatus is provided, focusing our attention to G-PISA experiment.

2   Instrumental Apparatus

We describe in the following the main characteristics of the experimental apparatus under study: the ring laser G-PISA, presently operating at the site of the Virgo gravitational wave interferometer, located in Cascina (Pisa, Italy). It consists in a helium-neon laser working on the red $474THz$ ($632.8nm$) line of neon; it operates in squared cavity having the side-length of $1.35m$ and the Earth rotation is enough to bias the Sagnac signal of the gyro well above the lock-in threshold.

The peculiarity of a middle size ring-lasers, as G-PISA, is to be transportable, and at the same time to reach an angular rate sensitivity at the level of some (nrad/s)/Hz in the seismic frequency range and to allow an almost continuous data taking. The experimental setup of the laser gyroscope is shown in the pictures of Fig.1.3 , in the two possible operational configurations for the measurement of the vertical and horizontal rotations. A 180 mm thick and $1.50m$ in side square granite slab sustains the whole mechanical ring and defines the laser cavity reference frame. A steel armed reinforced concrete monument has been designed and realized, which is able to sustain the granite table both horizontally and vertically, in order to measure the rotations around the vertical, or around the horizontal direction. A steel flange is embedded at the center both of the upper side and of the lateral side of the concrete monument, in order to firmly hold the granite table. The weight of the concrete monument is about 2 ton, while the granite table is about 1 ton. The weight of the whole structure has to guarantee a good contact with the floor. In order to improve this contact as much as possible, a liquid, fast-setting, concrete has been used to fill cracks and gaps between the floor and the monument basis. The scale factor of this is of $\simeq 0.0096 \ arcsec/count$.

The optical cavity which is based on the GEOSENSOR project [9], is enclosed in a vacuum chamber entirely filled with the active medium gas. The vacuum chamber has a stainless steel modular structure: 4 boxes, located at the corners of the square and containing the mirror holders inside, are connected by pipes through flexible bellows, in order to form a ring vacuum chamber with a total volume of about $5 \cdot 10^{-3} \text{m}^3$. The mirrors are rigidly fixed inside the boxes, which are rigidly fixed to the granite table. The mirrors alignment can be adjusted thanks to a micro-metric lever system that allows to regulate the two tilt degrees of freedom of each box. The typical measured ring-down time of

the light in the cavity made of super-mirrors is approximately 0.5 ms, giving an effective optical cavity quality factor of $Q = 2\pi f_0 \cdot \tau \sim 10^{12}$, providing a mirror reflectivity of $R = 99.9995$ % and a corresponding value for the losses per round trip $\mu_r = 2\pi f_0/Q_c$ of the order of some ppm . A fine movement of two opposite placed boxes along one diagonal of the square is also possible. This is provided by two piezoelectric transducers that allow the servo control of the laser cavity perimeter length. No window delimits the active region and the vacuum chamber is entirely filled with a mixture of He and a 50% isotopic mixture of ^{20}Ne and ^{22}Ne. The total pressure of the gas mixture is set to 560 Pa with a partial pressure of Neon of 20 Pa. The active region is contained in a Pyrex 4 mm diameter tube, where a plasma is generated by a RF capacitive discharge; the Pyrex capillary is inserted at the middle of one side of the ring. Getter pumps are used to keep low the hydrogen contamination of the active gas.

The capacitive coupled discharge is a peculiarity of the G-PISA apparatus. A capacitor made by two (semi) cylindrical electrodes (length of 2 cm) surrounds the Pyrex tube of the laser (see picture 2.1). This capillary has an internal diameter of 4 mm. No electrodes are required inside the tube. A radio-frequency power source (a voltage controlled oscillator or VCO) is used to power the capacitor and thus the discharge in the gas in the tube. The amplified VCO output is separated and send, in counter phase, to the two capacitor plates. This RF discharge is designed to be symmetrical, ensuring the maximum coupling between the field and the gas and minimizing any non- reciprocal effects (e.g., Langmuir flow) that can bias the Sagnac frequency. (That is why it is preferred to direct current, DC, excitation). The typical power of a single output beam is around 10 nW.

The signals of interest are sampled after being retrieved using trans-impedance photo diodes. The most reliable way to obtain Sagnac signal in G-PISA is superimposing the two beams in air, using an intensity beam splitter cube. This is done with the $+$ and $-$ beams exiting from on corner of the cavity. The cube is carefully aligned to combine the beams approximately with the same intensity (see the optical scheme in Fig.2.2). The interferogram signal is recorded by a photo-diode (PD) loaded on a trans-impedance amplifier. The photo-diodes are protected from the environmental light noise by interferential filter centered around 633 nm and having a bandwidth of few nanometers. The trans-impedance amplifier dedicated to the Sagnac signal detection provides a
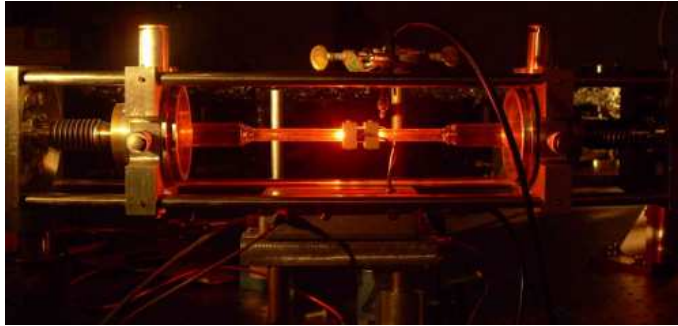
Figure 2.1: The G-PISA ring laser discharge excitation system.
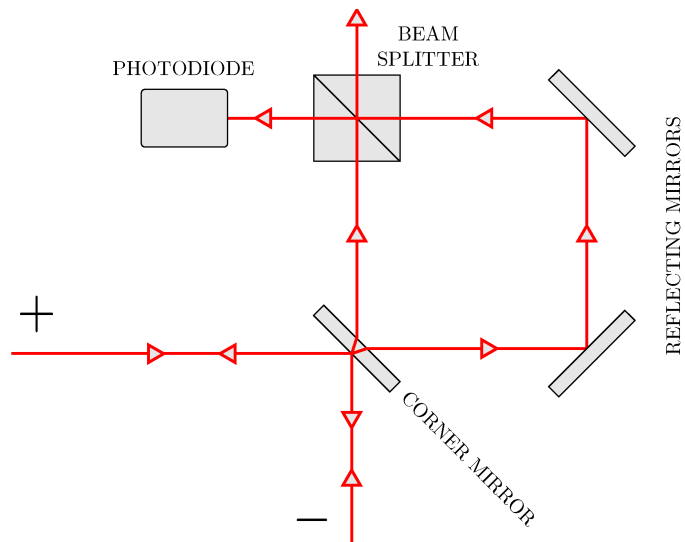
Figure 2.2: The optical scheme for the Sagnac interference frequency readout. +, clockwise beam; − counter-clockwise beam; M corner super-mirror; RM, mirrors used for beam-steering; BS, 50 : 50 beam-splitter; PD, photo-diode.
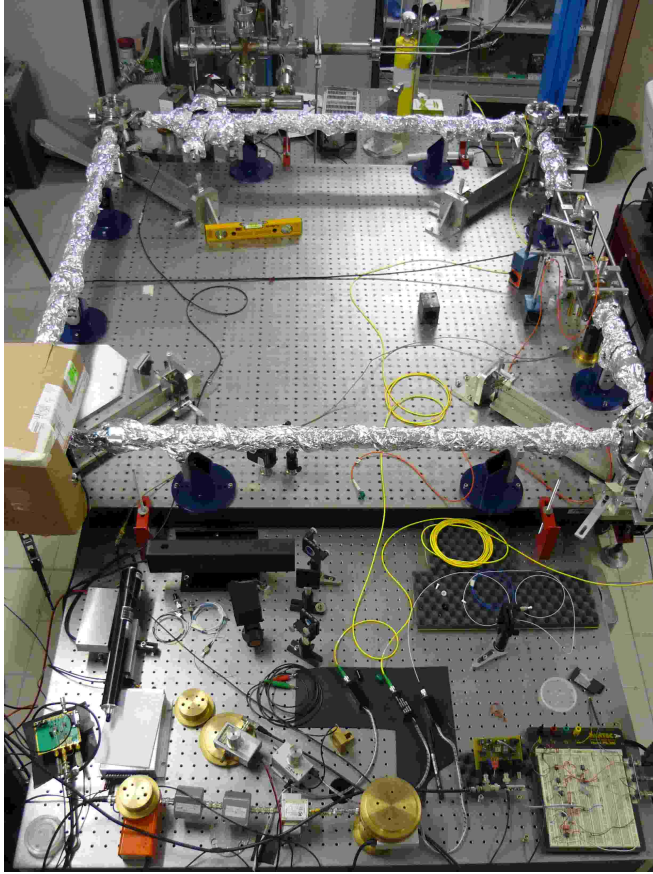
Figure 2.3: G-PISA Device

10^9 V/A gain with a rise time of 0.25 ms. It grants both the amplification and fast response required to detect the Sagnac signal of the weak output of gyro laser. Two identical, home made, trans-impedance amplifiers with a gain of $2 \cdot 10^9$ V/A and a rise time of 1 ms are used to detect the single-beam intensities for the + and the − beams.

2.1 Description of Stabilization loops

2.1.1 Perimeter Digital Control

The cavity perimeter is controlled by comparing the gyro laser optical frequency with a reference laser which is frequency-stabilized to the Doppler broadened

profile of the laser transition. The correction is applied to the ring cavity by acting on the piezoelectric devices moving the mirrors boxes. The frequency separation between the reference laser and the + laser beam is measured with a Fabry-Perot spectrum analyzer and the ring laser perimeter length is corrected in order to keep this difference equal to approximately 60 MHz, which corresponds to the cavity free spectral range and to the effective maximum of the gain curve as determined by the superposition of the Doppler broadened gain curves of ^{20}Ne and ^{22}Ne (The long term stability of the reference laser is given of the order of $1 - 2$ MHz over one year [10]).

The control scheme is sketched in Fig.2.4[10]. Both the radiations emitted from the gyro laser and the reference laser are injected into an optical fiber and superimposed in a two-fibers combiner. The output of the fiber coupler is mode-matched to a scanning Fabry-Perot analyzer with a free spectral range of 300 MHz, and a finesse of about 100, then the transmitted intensity is detected by a photomultiplier. The Fabry-Perot cavity length is constantly scanned by driving the piezoelectric transducer with a triangular waveform twice per second. After each scan the Fabry-Perot optical spectrum, containing the resonance peaks of the reference laser and the + beam one, is processed by a computer and the positions of the two peak centers are estimated via a parabolic fit of the data around the two transmission maxima. Once the resonances positions are estimated, a double digital PID feedback loop, acting on the gyro laser cavity length and on the offset voltage of the Fabry-Perot PZT, is then implemented using two independent DAC channels. Both PIDs have a predominant integral behavior with an integral gain close to the unity. The proportional and derivative gains have much lower values and are tuned to maximize the loop stability. To compensate the thermal drift of the analyzer cavity length the offset voltage of the Fabry-Perot ramp is actively controlled keeping constant the position of the reference laser resonance peak with respect to the starting value of the ramp.

The perimeter control implemented provides stable operations of G-PISA and it is necessary for minimum optical alignment requirements against laser frequency drifts over long time periods: in fact, laser can be affected by multimode transition phenomena. However, the laser behavior has been found to be quite stationary with occasional mode jumps reabsorbed after a while; nevertheless, when one of the two wave perform a mode jump, as long as laser remains in multimode regime, the inertial rotation information is lost. Unfortunately, this feedback produces a variation on the position of two opposite mirrors of the cav-

15
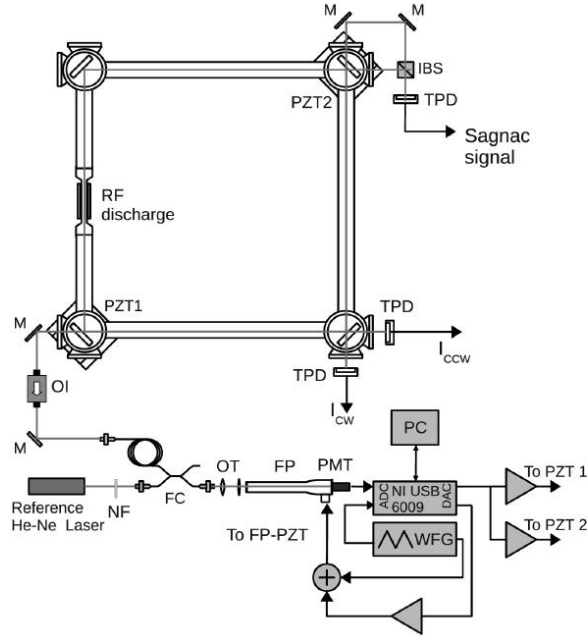
Figure 2.4: Experimental set-up of the perimeter-controlled gyro laser. The optical elements for the detection of the rotation signal (Sagnac signal) and of the clockwise and counterclockwise intensities (I_+ and I_-) is also shown. FP: Fabry-Perot analyzer, M: mirror, IBS: intensity beam splitter, TPD: trans impedance photo diode, PMT: photomultiplier, OI=optical isolator, FC: fiber coupler, NF: neutral filter, OT: optical telescope, PZT: piezoelectric transducer, WFG: waveform generator.

ity, resulting in many undesired effects (see Section 3) as changes in the effective area of the ring, changes in losses of the mirrors, etc. In fact, when the effective perimeter is locked to a fixed value, the geometry of the ring deviates from ideal square, leading to changes in the scale factor. However, considering that the RLG cavity is close to a perfect square (construction mechanical tolerances of about 1 mm) the relative change in the diagonal does not produce appreciable effects on the Sagnac frequency. In fact, since the temperature dependence of the perimeter length has been estimated as 30 $\mu m/K$, the error in the rotation rate due to the geometrical deformation of the RLG's cavity has been estimated at the level of 3 $prad/s/K$ [10].

16

Figure 2.5: Block diagram of the clockwise intensity I_+ stabilization system.

2.1.2 Clockwise Intensity Stabilization Loop

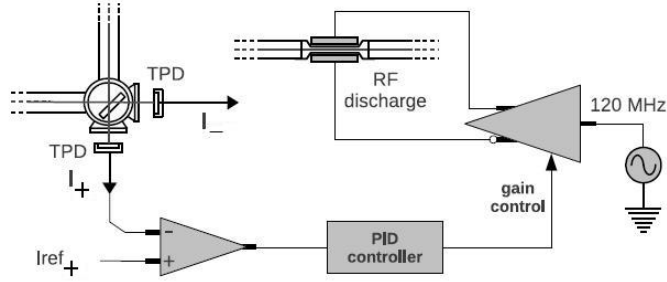The intensities of the light of the two counter propagating beams are influenced by several factors. On the one hand, an amplitude modulation at the Sagnac frequency is present, produced by back-scattering. On the other hand, the long term stability of the mean intensity is affected by factors like the optical mis-alignment in the light path, the variation of the RF power discharge, and the variations in the composition of the gas inside the cavity. As a first consideration, there are upper and lower limits for the beam intensities that should not be exceeded. The upper limit corresponds to the transition to multimode regime, while the lower limit is imposed by the laser threshold condition. Moreover, minor variations of the beam intensities not related to the Sagnac effect should also be avoided, as they induce undesired optical gain modulation and non-linear optical dispersion effects, as discussed in Section 3. In order to reduce undesired intensity fluctuations, a closed-loop stabilization system based upon a PID analog controller is implemented in G-PISA, as sketched in Fig.2.5. The input of the system is the intensity of the $'+'$ beam as revealed by the photo diode trans-impedance amplifier and integrated by an analog device; then the resulting signal is compared with an external reference intensity value. The output voltage of the PID controls the power of the RF plasma excitation through a variable gain RF amplifier, closing the loop. Note that the integrated signal is, in principle, not sensible to modulations. The laser amplitude stabilization reduces the long-term fluctuations, and increase the duty cycle of the apparatus, avoiding multi-mode behavior and switching-off of the laser.
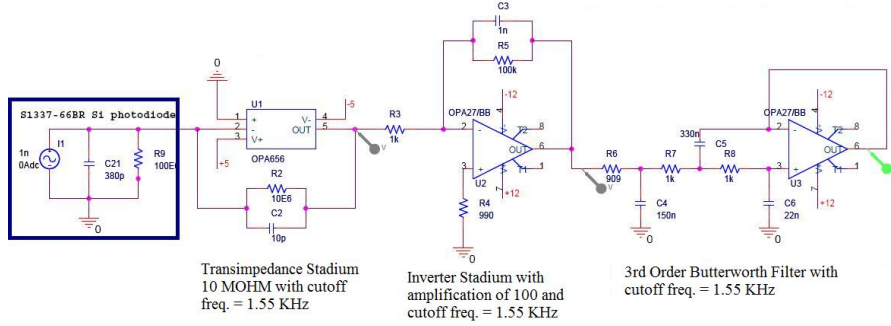
17

Figure 2.6: Intensity Detectors Amplification Stages

2.2 Data Acquisition

The data from the gyro laser are acquired and stored continuously by the data acquisition system provided by the VIRGO experiment [10]. The interferogram signal $\{S(n)\}$, $n \in \mathbb{Z}$ and the two mono-beam intensities $\{I_\pm(n)\}$ are acquired at the rate of 5 $kSample/s$ so that it is possible to reconstruct the Sagnac phase nominally up to 2.5 kHz. A local PC provides the evaluation of the instantaneous Sagnac frequency as well as of intensities $I_\pm$ at the rate of 1 Hz to provide estimations of rotation rate and the relevant parameters for the on-line monitor of the laser parameters dynamics. Some auxiliary channels are acquired at 1 Hz sample rate to complete the monitor of the G-PISA status (e.g. loop signals and mean intensities) and environmental disturbances (e.g. local tilts). A clock with an excellent long term stability (locked to GPS time) is used for the data acquisition timing process. The amplifiers involved in the main data acquisition process are three: one for the Sagnac signal and two for the beams intensities, the first is the LCA-4K-1G model by Femto [11] and its principal features are a gain of 10^9 Ω and a cutoff frequency of 4 kHz. Other two are homemade amplifiers and are designed for an high gain I-V conversion stage with low phase distortion, their gain is 10^9 Ω and their frequency response is a 5th order Bessel response with cutoff frequency of 1 kHz. The three photo diodes used for data acquisition are $S - 1337 - 66BR\ Si\ photodiode$ [12], designed for high sensitivity and low capacitance.

3 Modeling the measurement process

In this section we discuss the equations that describes the RLG dynamics. We consider the so called "Fundamental limit of rotational sensitivity" as a model of the component of measured error relative to laser light incoherence; then the dynamic equations regulating the two mono-beam intensities and the phase difference are derived, illustrating the procedure used and the corresponding approximations. Finally, the parameters that appear in the equations are analyzed and the parametric identification procedure presented.

3.1 Noise Quantum Limit

A fundamental limit of rotation sensitivity of a RLG is set by Quantum Optics. A semi-classical formalism is usually introduced to define this source of noise, and it has been shown that the noise affecting Sagnac frequency is white and caused by spontaneous emitted photons. That noise source integrated over time leads to angular random walk (red noise or $1/f^2$ noise) [13]. Quantum RLG noise has been studied more carefully using quantum formalism (see e.g. [7, 15]). These models widely differ each other for scale factor and ad-hoc corrections, basing on different instrumental device, despite some agreement has been obtained [7, 13, ?]. Derivations leads to the following expression for the random walk coefficient, which rely on the fact that the minimum detectable rotation rate is proportional to the inverse square root of the mean photon number with coherent phase

$$\delta\Omega = \frac{SF \cdot c}{Q\lambda} \sqrt{\frac{hf_0}{Pt}} \; rad/s/\sqrt{Hz} \qquad , \qquad (3.1)$$

where h is the Planck constant, P the total beam power in the cavity and t observation time. Common values of this index for large RLG are $10^{-10} \div 10^{-11} \; rad/s/\sqrt{Hz}$ at $\sim 1 \; Hz$. This source of noise in commercial RLG is considered of secondary importance with respect to other sources of noise, while the noise level in large RLG approached the fundamental limit in Eq.(3.1) on $10^{-1} \sim 10^{-3} \; Hz$ band. However for long times, i.e. very low frequencies $10^{-3} \div 10^{-5} \; Hz$, this limit has not yet been achieved. We think that the fundamental limit in Eq.(3.1) could be achieved using EKF techniques.

A statistical noise analysis of the quantum noise can be performed basing on stochastic processes models. Consider a laser beam, theoretically phase coherent: spontaneous photons with random phase are emitted at random. The presence of these photons determines uncertainties in photo detector as long as emitted photons lives in the cavity. When the laser pump trough the cavity, few photons emissions, compared to the ones with coherent phase, makes phase incoherent. However this phenomena has been experimentally observed to be stationary at the detection frequency, and being the photon lifetime in the cavity $\sim 1\ ms$, after the instrument is operating for several hours a constant amount of the laser photons manifests a frequency error at the detector. Furthermore the absolute number of emitted photons is high, so central limit theorem holds, see ref. [16, 18].

3.2 The ring laser dynamics

The dynamic equations describing the RLG behaviors can be found in the framework of the Lamb formalism [17], which requires the following assumptions:

i)   the two oppositely directed traveling waves in the cavity have independent amplitude and phase;

ii)   an electromagnetic field exist in the cavity and the electric component of the field leads to macroscopic atom polarization.

By using Maxwell's equations on the rotating cavity frame with the polarization as source, the electromagnetic field interaction with atoms is determined and, for self-consistency, equalized to the starting field. The Maxwell's equations are then solved by means of a perturbative method, which consists in a third order expansion of the density matrix in powers of interaction between the radiation field and the atomic system. This method is experimentally justified if the laser is operated near threshold condition[17]. The resulting equations read

$$\frac{2L}{c}\frac{\dot{E}_+}{E_+} = \alpha_+ - \beta_+\sqrt{E_+} - \theta_\pm\sqrt{E_-} - 2r_-\frac{E_-}{E_+}\cos(\Psi + \varepsilon_-)$$

$$\frac{2L}{c}\frac{\dot{E}_-}{E_-} = \alpha_- - \beta_-\sqrt{E_-} - \theta_\mp\sqrt{E_+} - 2r_+\frac{E_+}{E_-}\cos(\Psi - \varepsilon_+) \qquad (3.2)$$

$$\omega_+ + \dot{\phi}_+ = \Omega_+ + \sigma_+ + \tau_\pm\sqrt{E_-} - \frac{c}{L}r_-\frac{E_-}{E_+}\sin(\Psi + \varepsilon_-)$$

$$\omega_- + \dot{\phi}_- = \Omega_- + \sigma_- + \tau_\mp\sqrt{E_+} - \frac{c}{L}r_+\frac{E_+}{E_-}\sin(\Psi - \varepsilon_+) \qquad ,$$

where $E_\pm$ is the electric field intensity, $\phi_\pm$ arbitrary phase angles for the corresponding wave, $\Psi = \phi_- - \phi_+$, $\omega_\pm$ are the oscillation frequencies, $\Omega_\pm$ the natural frequencies of the cavity involved in Sagnac effect, $\alpha_\pm$ the excess gain minus losses, $\beta_\pm$ the pure saturation terms, $r_\pm$ is the scattering coupling coefficients, $\varepsilon_\pm$ the scattering phase angles, $\sigma_\pm$ the scale factor error parameters of the $+$ and $-$ beam, respectively. Here $\theta_{\pm,\mp}$ are the cross saturation terms and $\tau_{\pm,\mp}$ the null-shift error parameters.

Those equations are recast by expressing the electric field amplitudes as a function light intensities (i.e. $I_\pm \propto E_\pm^2$), defining $\varepsilon = (\varepsilon_+ + \varepsilon_-)/2$, and expressing the phase difference as $\Psi = \psi + (\xi_+ - \xi_-)/2$. Finally the oscillation frequencies $\omega_\pm$ are supposed equal for both waves. We obtain the set of equations:

$$\dot{I}_+ = \frac{c}{L}\left(\alpha_+ I_+ - \beta_+ I_+^2 - \theta_\pm I_+ I_- + 2r_-\sqrt{I_+ I_-}\cos(\Psi + \varepsilon)\right)$$

$$\dot{I}_- = \frac{c}{L}\left(\alpha_- I_- - \beta_- I_-^2 - \theta_\mp I_+ I_- + 2r_+\sqrt{I_+ I_-}\cos(\Psi - \varepsilon)\right) \qquad (3.3)$$

$$\dot{\psi} = \omega_s + \sigma_- - \sigma_+ + \tau_\mp I_+ - \tau_\pm I_- -$$

$$- \frac{c}{L}\left(r_+\sqrt{\frac{I_+}{I_-}}\sin(\psi - \varepsilon) + r_-\sqrt{\frac{I_-}{I_+}}\sin(\psi + \varepsilon)\right) .$$

where $\omega_s = \Omega_- - \Omega_+$. We point out that only a single laser mode is considered in this approximation and, in addition, $I_\pm$ and ψ are assumed to slowly vary in time compared to $\omega_\pm$. When the laser is not in the ideal working conditions and/or the cavity ideality is not satisfied, Eqs.3.3 no more hold. However, the perimeter control of G-PISA ensures mono-mode and stable operations.

3.2.1 Back-scattering Phenomena

The most important contribution to systematic error on RLG frequency estimation in the model is due to the back-scattering effect[10, 7].

Considering the standard literature approach, the frequency detection present a source of error due to nonlinear coupling therms in Eqs.(3.3):

$$\omega_{BS} = -\frac{c}{L}\left(r_+\sqrt{\frac{I_+}{I_-}}\sin(\psi - \varepsilon) + r_-\sqrt{\frac{I_-}{I_+}}\sin(\psi + \varepsilon)\right) \qquad (3.4)$$

This systematic error is not a pure sinusoidal signal. The non-linear dynamics and the variation in time of the parameters make this error not computable with a simple average. The EKF, which has been devised for non-linear and time-varying systems, should be able to remove this effect from the phase dynamic.

To better discuss the back-scattering we deal with the geometrical description of the phenomena. With reference to Fig.3.1 the phasors, representing the mono-beam electric field, are rotating with respect to an inertial frame; a portion of each beam, supposed to be constant and equal for the two beams, is added to the other beam, as prescribed by Eq.(3.3).Two different dynamical regimes of the RLG occur [7].

i)   *Dissipative Coupling:* $\varepsilon = 0$; the phasor addition, as a function of the scattering angle ε, is symmetric, the intensities fluctuations are in-phase and the error on the frequency is maximum, this happens because the phasor phase difference become smaller and higher when the two phasors rotates.

ii)   *Conservative Coupling:* $\varepsilon = \pi/2$, the phasor addiction is asymmetric, the intensities fluctuation are in antiphase and the frequency error is minimum because the back-scattering contributions add up on the two phasor in the same direction, thereby not changing their phase difference.

The phasor model has been accurately tested for RLG back-scattering [17, 7], and also validated if scatter phasors amplitudes have different magnitude. The scattering phenomena introduces a sort of dead zone in RLG dynamic, that result in a lock-in threshold ω_L. For rotation rate higher than the threshold,
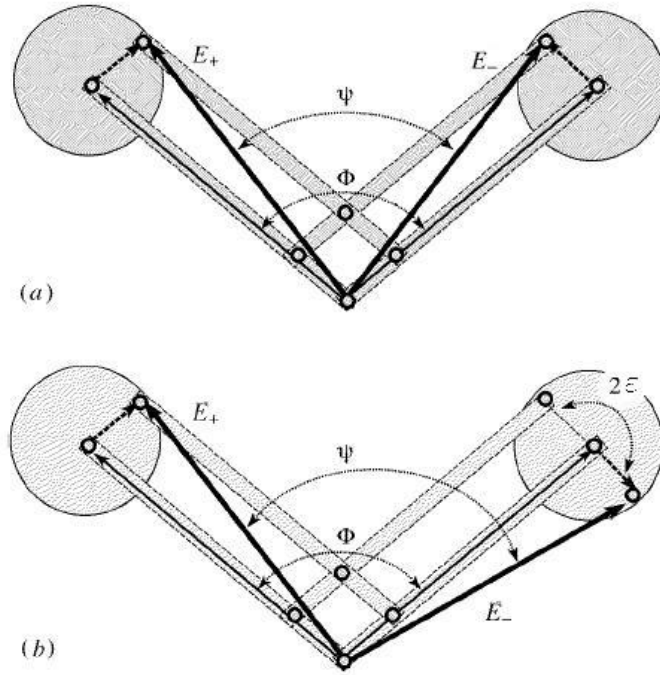
Figure 3.1: Phasor diagrams for describing back-scattering. A proportion (dashed vector) of one beam phasor (thin solid vector) is added to the other, indicating the time development of the final phasors $\widetilde{E}_+,\widetilde{E}_-$ (thick solid vectors). In the absence of scattering, moduli would be constants and phase Φ would increase in time linearly; Ψ is this phase adjusted for back-scattering. (a) Dissipative coupling, (b) Conservative coupling .

the lock-in effect has been discussed in the phasor model, and it results in a systematic detection error. On the other hand, when the imposed rotation rate is near ω_L the laser dynamic locks to a steady state solution, as the relative frequency of back-scattered beams is comparable to Sagnac signal contribute, and the information concerning rotation is lost.

For this reason RLG have been implemented trying to reduce mirror scattering, and thus lock-in operation region. Another solution to avoid the lock-in problem was to dihter the RLG itself with a rotating platform, (e.g. ref.[17]).

For G-PISA the coupling is actually mostly dissipative, and lock-in threshold $\sim 10\ Hz$ is well under the Sagnac frequency that corresponds to earth rotation rate $\sim\ 100\ Hz$, so the system is naturally always unlocked.

3.2.2   Lamb Formalism for laser Constants

Laser constants can be calculated using the standard approach in the literature, namely the Lamb formalism [21].

We start from the proportionality factor between electric fields $E_\pm$ and laser mono-beam intensities $I_\pm$

$$I_\pm \ = \ \frac{|\mu_{ab}|^2}{2\hbar^2\gamma_a\gamma_b}E_\pm^2 \ = \ \frac{|\mu_{ab}|^2}{2\hbar^2\gamma_a\gamma_b} \cdot \frac{P_{out}}{2c\epsilon_0\mathcal{A}T} \qquad , \qquad (3.5)$$

where μ_{ab} is the element of the electric dipole laser matrix between laser states a and b (i.e. the upper and the lower of the laser energy levels), $\gamma_{a/b}$ are the decay rates of those levels in units of Hz, $\eta = \gamma_{ab}/\Gamma_D$ is the ratio between homogeneous and Doppler broadening in the laser composition, $\gamma_{ab} = (57p + 10)\ MHz$ is the homogeneous broadening made of radiation decay rate plus collision induced rate by the two levels, and $\hbar$ is the reduced Plank constant. Here Γ_D is the Doppler broadening frequency (the spontaneous emission atomic frequency of the cavity), p is the effective gas pressure near the mirror in $Torr$; P_{out} is the output power measured in W, ϵ_0 is the dielectric constant of vacuum, $\mathcal{A}$ is the area of the transverse section of the beam in m^2, T is the transmission coefficient of the mirror expressed in ppm.

The electric dipole element μ_{ab} can be written in term of fundamental physical constants,

a	$3s2$
b	$3p4$
λ	$0.63281 \cdot 10^{-6} m$
γ_a	$8.35 \cdot 10^6 Hz$
γ_b	$9.75 \cdot 10^6 Hz$
A	$\pi \cdot 2.59 \cdot 2.26 \cdot 10^{-6} m^2$
A_{ik}	$3.39 \cdot 10^6$
T	$1\ ppm$
p	$5\ Torr$
P	$3 \cdot 10^{-9} W$
Γ_D	$2\pi \cdot 10^9 MHz$

Table 3.1: Table with G-PISA laser parameters.

$$\mu_{ab} = \sqrt{\pi \epsilon_0 \frac{\lambda^3}{(2\pi)^3} \hbar A_{ik}} \qquad , \tag{3.6}$$

where A_{ik} is transition rate between the laser levels.

The laser parameters for G-PISA are summarized in Tab3.1, and by means of constants in Tab. 3.1 we get:

$$\begin{aligned} \gamma_{ab} &= & 295\ MHz \\ \eta &= & 0.047 \\ \mu_{ab} &= & 3.188 \cdot 10^{-30} C\,m \end{aligned} \qquad . \tag{3.7}$$

The coefficients in Eq.(3.3) can be calculated by means of the plasma dispersion function, i.e. the function associated to the broadening profile of the laser transition[21]

$$Z(\xi) = 2i \int_0^\infty e^{-x^2 - 2\eta x - 2i\xi x} dx \qquad . \tag{3.8}$$

The derivation of $Z(\xi)$ follows from an experimental approach, and describes well lasers designed to be mainly Doppler broadened, as G-PISA. For others gas mixture the plasma dispersion function can vary according to ref.[9]. Here $\xi_\pm = (\omega_\pm - \omega_0)/\Gamma_D$ are a quantification of the laser frequency detuning of the $\pm$ beams from cavity center frequency (free spectral range in units of pulsation ω_0) normalized to the Doppler width, note that ω_+ is the quantity stabilized by the perimeter control loop in G-PISA. Reference values for $\xi_\pm$ are $\sim 10^{-7}$.

The independent variables $\xi_\pm$ are in correlation with temperature and pressure inside the cavity.

In case of Doppler limit $\eta \ll 1$, which is common for large size $He - Ne$ RLG, $Z(\xi)$ is usually approximated as follows

$$
\begin{aligned}
Z_I(\xi) &\simeq \sqrt{\pi} e^{-\xi^2} - 2\eta \\
Z_R(\xi) &\simeq -2\xi e^{-\xi^2}
\end{aligned}
\qquad , \qquad (3.9)
$$

where the subscripts R and I stands for imaginary and real part, respectively. With the above approximations the parameters of Eq.(3.3) become

$$
\begin{aligned}
\alpha_\pm &= G \cdot \frac{Z_I(\xi_\pm)}{Z_I(0)} - \mu_\pm \\
\beta_\pm &= \alpha_\pm + \mu_\pm \\
\sigma_\pm &= \frac{f_0}{2} \cdot G \cdot \frac{Z_R(\xi_\pm)}{Z_I(0)} \\
\theta_\pm &= \beta_- \cdot \frac{1}{1 + (\xi_+/\eta)^2} \\
\theta_\mp &= \beta_+ \cdot \frac{1}{1 + (\xi_-/\eta)^2} \\
\tau_\pm &= \frac{f_0}{2} \cdot \frac{\xi_+}{\eta} \cdot \theta_\pm \\
\tau_\mp &= \frac{f_0}{2} \cdot \frac{\xi_-}{\eta} \cdot \theta_\mp
\end{aligned}
\qquad (3.10)
$$

where G is the laser gain, and $\mu_\pm$ the mirror losses relative to the $\pm$ beams. We stress that $\xi_\pm$ and $\mu_\pm$ must be evaluated for each of the two beams, as the non reciprocity in the parameters values will lead to asymmetric effects on ψ and $I_\pm$, and thus to non-linear degradation of the rotation signal. The Sagnac effect itself forces the two mono-beam frequencies to differ of ω_s. To take into account the perimeter loop control in G-PISA, it is $\omega_+ \simeq \omega_0$, and so $\omega_- = \omega_S - \omega_0$.

3.2.3 Gain

The laser gain G is a parameter of paramount importance in RLG design. Its magnitude determines the laser behavior ranging from near threshold to multimode operation. The dependence of $\alpha_\pm$ and $\sigma_\pm$ on G is exactly determined,

26

instead the $\beta_{\pm\mp}, \theta_{\pm\mp}$ formulae as functions of G are most valid in the Doppler limit and near threshold; for instance for gain higher than threshold, the terms $\beta_\pm$ saturates themselves, allowing to the intensities (mean values) to grow linearly with the gain ($\beta_{G\rightarrow\infty} \rightarrow O(1)$ in contrast with Eq.(3.10)). Despite most of parameters are different for the two beams (thereby the use of $\pm$ subscripts), G has the same value in both intensity equations. The direct calculation of the gain can be performed by the observation of the mean level of the intensities: $<I_\pm> = \alpha\pm/\beta\pm$, then G can be obtained inverting Eq.(3.5). It is worth noticing that gain should be determined considering the broadened profile of the laser transition, as a function of f_0. However, near threshold cavity, G depends linearly from the RF amplification and its dependence on cavity free spectral range can be dropped.

The explicit gain calculation for G-PISA, with $\mu \sim 10^{-6}$, gives $G \simeq 1.013\cdot 10^{-6}$; its worth noticing that in G-PISA a servo-control acting on G is implemented. The servo-control signal allow us to measure explicitly the gain variations during G-PISA operation.

3.2.4 Diffusion and Diffraction Losses

Losses are mainly due to mirrors surface imperfections. In Section 2 we gave a formula for estimating the sum of the two cavity losses. However, we need to evaluate separately the two beam losses; further insights into the gain considerations and Eq.(3.10) suggest an easy way to estimate both losses.

The effects of $\mu_\pm$ accounted for in Eq.(3.3) are not the only known effects due to losses, as one can show [17] that the back-scattering phenomena is due to a sort of a.c. losses source (scattering), in contrast with d.c. losses source (transmission). To perform a raw calculation of the back-scatter magnitude, one can use the cavity quality factor to estimate the total losses $\mu = (1 - R^4) \simeq 4(1 - R) = 4(T + r_s)$, where $\mu = \mu_+ + \mu_-$, R is the mirror reflectance, T the mirror transmission and r_s is the mirror scattering coefficients. Scattering terms in Eq.(3.3) turn out to be $r_\pm = r_s\lambda/4d_\pm$; here $d_\pm$ is the beam diameter of the $\pm$ beams. However, non reciprocal parameter calculation cannot be performed using only ring-down time and quality factor.

For sake of completeness it must be also said that in our analysis ε is assumed to be a casual function of time. It has been shown that in most experimental

conditions for a RLG with no feedback ε is 0 (dissipative coupling) or $\pi/2$ (conservative coupling) [7]. From an experimental point of view, one can determine the magnitude of scattering angle of RLG with feedbacks by means of its effects on intensities [17, 19].

3.2.5 Logistic behavior

The role of the parameters $\alpha_\pm$ and $\beta_\pm$ on Eqs.(3.3) can be studied following an analogy with competition models in ecologic systems.

Without competition with others species, populations are assumed to saturate their number of individuals due to their intraspecific competition, instead of diverging exponentially. A simple model that describes this behavior is the Logistic Model [20]. Consider the atomic $He - Ne$ population, the atoms that propagates the beams $+$ and $-$ are treated as different populations in competition. In absence of extra-specific competition, according to Logistic Model, the growth of the two populations are described by:

$$\dot{I}_\pm(t) = \alpha_\pm I_\pm - \beta_\pm I_\pm^2 \qquad (3.11)$$

This model with positive parameters has two steady state solutions for each dimension, i.e. the unstable solution $I_\pm = 0$ and the stable solution $I_\pm = \beta_\pm/\alpha_\pm$. Obviously the null steady state refers to extinction and the positive one to asymptotic subsistence of population individuals. According to the logistic model $\alpha_\pm/\beta_\pm$ set the mean value of the laser light intensity of the $\pm$ beams.

3.2.6 Competition Coefficients

The competition coefficients $\theta_{\pm\mp}$ introduce a decrease in the laser mean intensity $I_\pm$ correlated to opposite beam magnitude $I_\mp$. This effect can be explained with the use of the Logistic Model extended to the presence of extra-specific competition, which reads

$$\dot{I}_\pm(t) = \alpha_\pm I_\pm - \beta_\pm I_\pm^2 + \theta_{\mp\pm} I_+ I_- \qquad . \qquad (3.12)$$

The two equations are now coupled, and some conditions on the equation parameters determine the existence of multiple steady state solution, as well as

their stability. Possible equilibrium solutions are 4: extinction of both popula-
tions, subsistence of one and extinction of the other and subsistence of both.
The form of RLG parameters leads to asymptotic stability of the population
coexistence case. Therefore the effect of the $\theta_{\pm,\mp}$ parameters is a decrease in
the mean asymptotic value of the laser intensities [20]. However, in the Doppler
limit $\eta \ll 1$, the presence of competitions coefficients is negligible for model-
ing. Moreover, it has been shown [10] that using two Ne different isotopes,
cross-saturation gas phenomena is completely negligible, leading to $\theta_{\pm,\mp} = 0$.

3.2.7   Frequency Parameters

In most of the literature the terms proportional to $\sigma_\pm$ and $\tau_\pm$ in the equation
for $\dot{\psi}$ are treated as systematic error sources. Their effect in the estimation of
the Sagnac frequency is taken into account by a first or second order expansion
in series of the Lamb quantities and $I_\pm$.

The presence of $\sigma_\pm$ in Eqs.(3.3) determine a frequency scale error, since they
are proportional to f_0 and homogeneous with ω_s. They are accounted in the
correction of the scale factor together with local tilts and perimeter changes.
The presence of any physical passive non reciprocity in the cavity (laser shut-
ter or cavity micro-holes, especially near RF discharge and gas dispensation
components) affect the RLG dynamic with the same effect as $\sigma_\pm$. However, the
presence of a term linear in ξ in their definition implies that they have a small
magnitude if $\xi \simeq 0$; in addition, the mentioned non-reciprocal effects have been
carefully avoided in the G-PISA design, and so their presence can be neglected
at a first approximation.

The $\tau_{\pm,\mp}$ are related to competition coefficients, and introduce competitive in-
tensities dynamics into phase dynamics. This contribute is gathered together
with gas flow and discharge effects, as they determine a null shift error in the
frequency estimation. However, Eqs. (3.10) shows that $\tau_{\pm\mp}$ are negligible if
$\theta_{\pm\mp} = 0$. Moreover, G-PISA is provided with a gas restorator and its operation
is free from gas flow effects.

3.3   Study of the Dynamical Equations

The typical parameters for G-PISA have been roughly estimated according to
the following considerations. Parameters $\alpha_\pm$ and $\beta_\pm$ are estimated from the out-

Parameter	$+$	$-$
α	$1.3 \cdot 10^{-8}$	$1.3 \cdot 10^{-8}$
β	$1.13 \cdot 10^{-6}$	$1.13 \cdot 10^{-6}$
θ	0	0
σ	0	10^{-6}
τ	0	0
r	$2 \cdot 10^{-7}$	$2 \cdot 10^{-7}$

Table 3.2: G-Pisa parameters

put power of both beams, using the logistic behavior steady state solution and Eq.(3.5), . The magnitudes of scattering coefficients $r_{\pm}$ are estimated considering the amplitude intensity modulation and the instantaneous Sagnac frequency range. $\theta_{\pm\mp}$ and $\tau_{\pm\mp}$ are set to 0 because different isotopes of Ne have been used [10]. The results we get are summarized in Table 3.2.

Due to the non existence of a general closed form solutions, the analysis of Eqs.(3.3) is very difficult. Closed form solutions exists if some conditions involving symmetries in Lamb coefficients holds [17, 7]. However, no closed form solution is found in the non reciprocal case, and so numeric integration is required.

3.3.1 Closed Form Solutions

The simplest closed form solution of Eq.(3.3) can be found using the Adler approximation; this solution has been studied in the literature since the first RLG came into operations [17]. To derive Adler equation one usually assumes equal back-scattering coefficient $r_+ = r_- = r$; here we derive a slightly different solution in the case of $r_+ \neq r_-$.

Consider the fundamental RLG equations if the parameters are very similar for the $+$ and $-$ beams, $\sigma_+ \simeq \sigma_-$, $\tau_+ \simeq \tau_-$, $I_+ \simeq I_-$ then the equation for the phase difference can be approximated as:

$$\dot{\psi} = \omega_s - \frac{c}{L} \left(r_+ \sin(\psi - \varepsilon) + r_- \sin(\psi + \varepsilon) \right) \qquad , \qquad (3.13)$$

and the Adler equation can be recovered from Eq.(3.13) in the $r_+ = r_- = r$ limit [17]

30

$$\dot{\psi} = \omega_s - \omega_L \sin(\psi) \qquad , \tag{3.14}$$

where $\omega_L = 2r\frac{c}{L}\cos(\varepsilon)$. The solution of the Adler equation reads

$$\psi(t) = 2\arctan\left\{ \frac{\Omega_L + \sqrt{\omega_s^2 - \omega_L^2}\tan\left[\frac{1}{2}(t-t_0)\sqrt{\omega_s^2 - \omega_L^2}\right]}{\omega_s} \right\} \quad , \tag{3.15}$$

Eq.(3.14) clearly describes the lock-in phenomena we previously addressed to, in the case of symmetric scattering.

After some elementary algebra Eq.(3.3) can be recast as:

$$\dot{\psi}_- = \omega_s - \frac{c}{L}(r_+ + r_-)sin(\psi - \varsigma) \qquad , \tag{3.16}$$

where $\varsigma = \arctan\left(\frac{r_+ - r_-}{r_- + r_+}\tan(\varepsilon)\right)$, and its solution read

$$\psi(t) = 2\arctan\left\{ \frac{(\rho_+ + \rho_-)\cos(\varepsilon) + \sqrt{\omega_s^2 - \omega_L^2}\tan\left[\frac{1}{2}(t-t_0)\sqrt{\omega_s^2 - \omega_L^2}\right]}{\omega_s + (\rho_- - \rho_+)\sin(\varepsilon)} \right\} \quad , \tag{3.17}$$

where $\rho_\pm = r_\pm \cdot c/L, \qquad \omega_L^2 = \rho_+^2 + \rho_-^2 + 2\rho_+\rho_-\cos(2\varepsilon)$, and t_0 is an integration constant that can be fixed by imposing initial conditions, e.g.

$$\psi(t_0) = 0 \Longrightarrow t_0 = \frac{-2\arctan\left[\frac{(\rho_+ + \rho_-)\cos(\varepsilon)}{\sqrt{\omega_s^2 - \omega_L^2}}\right]}{\sqrt{\omega_s^2 - \omega_L^2}} \quad . \tag{3.18}$$

3.3.2 RK-4 Routine

The numerical integration of Eqs.(3.3) can be carried out by means of 4th order Runge-Kutta method [?].

Let an initial value problem be specified as follows

$$\dot{y} = f(t, y), \quad y(t_0) = y_0 \tag{3.19}$$

Then, the RK4 method for this problem is given by the following equations:

$$y_{n+1} = y_n + \frac{\Delta t}{6}(k_1 + 2k_2 + 2k_3 + k_4) \tag{3.20}$$

$$t_{n+1} = t_n + \Delta t \quad , \tag{3.21}$$

where y_{n+1} is the RK4 approximation of $y(t_{n+1})$, and

$$k_1 = \Delta t \cdot f(t_n, y_n) \tag{3.22}$$

$$k_2 = \Delta t \cdot f(t_n + \frac{\Delta t}{2}, \ y_n + \frac{\Delta t}{2}k_1) \tag{3.23}$$

$$k_3 = \Delta t \cdot f(t_n + \frac{\Delta t}{2}, \ y_n + \frac{\Delta t}{2}k_2) \tag{3.24}$$

$$k_4 = \Delta t \cdot f(t_n + \Delta t, \ y_n + \Delta t k_3) \quad . \tag{3.25}$$

Thus, the next value y_{n+1} is determined by the present value y_n plus the weighted average of k_i, where each delta is the product of the size of the interval Δt and an estimated slope $h_{slope} = \Delta t(dy/dt) = \Delta y$.

k_1 is based on the slope at the beginning of the interval, using y_n (Euler's method); k_2 is based on the slope at the midpoint of the interval, using $y_n + \Delta t \cdot k_1/2$; k_3 is again based on the slope at the midpoint, but now using $y_n + \Delta t \cdot k_2/2$; k_4 is based on the slope at the end of the interval, using $y_n + \Delta t \cdot k_3$. In the average greater weight is given to the k_i evaluated at $t_n + \Delta t/2$.

The RK4 method is a fourth-order approximation method, meaning that the error per step is on the order of Δt^5, while the total accumulated error has order Δt^4 if the equations are not stiff. Note that the above formulas are valid for both scalar- and vector-valued functions (i.e., y can be a vector and $f(t, y)$ an operator). The integration error of the RK-4 routine has shown to increase with time if applied to non-stationary stiff equation systems [22]; RLG equations are found to be stiff, consequently the integration error on the phase difference increases with time. This source of error introduce a constraint on the numerical

32

simulation time length. However, in the EKF prediction step RK-4 integration error will be on the magnitude of 10^{-15}, thus negligible at a first approximation for the purpose of implementing an EKF.

3.4 Combined control loop dynamics

In this section we study the effects of the two control loops on the fundamental RLG equations that have been derived without considering feedbacks. The main feedback implemented in G-PISA i.e. the perimeter stabilization prevent the laser to switch off and to preform mode jumps. The stabilization of the optical frequency is one of the conditions that allow us to derive the RLG equations; moreover, the free spectral range and the laser detuning frequencies determine the magnitude of the Lamb coefficients. In Eqs.(3.3) the factor c/L can be assumed to be constant thanks to perimeter digital control, so we have implicitly accounted for one feedback effect. The other feedback, i.e. the I_+stabilization, is responsible for the gain variations. In general we can conclude that the actions of these feedbacks introduce time-varying behaviors in some RLG parameters while rejecting variations in some others.

3.4.1 Perimeter Stabilization

To derive a model for the feedback of the perimeter control, the dynamic of this loop is now further analyzed. We stated before that optical cavity frequency is normally affected by thermal and pressure changes. Thermal expansion of the cavity determines a shift of the beam spot positions on mirrors, leading to changes in the detuned laser frequencies (from cavity optical one) that depends on mirror micro-shape in the spot neighborhood and in the cavity shape itself. We must remark that the detuned frequency difference is kept constant by Sagnac effect itself, and that temperature and pressure values are thought as the aggregate expression of temperature and pressure distribution in the cavity. The expansion can bring the laser to unstable behavior. For this reason it is stabilized the cavity optical frequency $+$. In standard loop conditions the frequency of loop operation is sufficiently high if compared to detuned frequency drift one, but it is low if compared to the optical frequency $\omega_+ \simeq 50MHz$ and also to the beat frequency $\omega_s \simeq 100Hz$. Therefore the loop on the free laser spectral range rejects variations inducted by temperature and pressure without modifying the dynamics.

However, the feedback scheme presented has some disadvantages and undesired effects: experimental work on G-PISA, has shown that the beat signal and the intensities are a.c. modulated by piezo action if the piezo correction is applied to only one mirror. Actual loop design of improved symmetry has outcome this problem by using two piezo acting on the mirrors. On the other hand, feedback action produces a drift in Lamb parameters $\mu_\pm$, $r_\pm$, and ε over time scale of seconds. In fact, if the RLG cavity perimeter is changed by piezo, light spots move on mirrors leading to beam path variations. Those variations determine a random change of $\mu_\pm$, $r_\pm$, and ε. In addition, the loop allows small drifts of the optical detuned frequency on the $1\ Hz$ scale. From Eq.(3.10), if the detuned optical frequencies randomly changes, then the laser dispersion function changes and thus the parameters of the laser dynamic change.

Following the model the effects we have to take in account for simulation purpose is the addition of $1\ Hz$ noise in $\xi_\pm$, and of random walk processes to $\mu_\pm$, $r_\pm$, and ε. As at the beams generation frequencies $\sim f_0$ the feedback does not work, $\xi_\pm$ noise whiteness holds. This noise process is kept stationary by the perimeter feedback in the $1\ Hz$ time scale, and process variance is determined by the temperature and pressure action on the characteristic loop times, leading to very small values.

In the day selected for experimental considerations we recorded a maximum detuning $+$ variation of $\Delta\omega_+ \sim 5\ MHz$, and exploiting relations of Section 3 we estimate a maximum detuning $-$ variation of $\Delta\omega_- \sim -5\ MHz$. These variations are consistent in a maximum change on the ratio $\xi_\pm$ of $\sim 10^{-3}$. The corresponding change in the therms $Z_I(\xi_\pm)/Z_I(0)$ and $Z_R(\xi_\pm)/Z_I(0)$ in Eqs.(3.10) leads to relative variation for logistic parameters $\alpha_\pm, \beta_\pm$ of 10^{-7} and of 10^{-4} for $\sigma_\pm$. Therefore the experimental detuning drift allowed by the perimeter loop is negligible in the Lamb coefficients determination. Computed $\beta_\pm$ variation are small, moreover the only asymmetric contribution in $\beta_\pm$ expression is due to $\xi_\pm$. Therefore we drop the $\pm$ notation for β, and we assume from now on that the change in $\xi_\pm$ at closed loop operation is negligible for G-PISA.

3.4.2 Intensity Stabilization

The mean value of intensities is determined to good approximation by gain and losses. The control of the perimeter introduces random behavior in losses, thus (basing on logistic model and Lamb derivation) affecting the long therm

stability of light intensities. For this reason the + intensity control loop has been implemented. It acts on the analogical integrated I_+ signal, comparing it with a reference laser (Section 2). The sinusoidal part of the intensity is not changed by the feedback action thanks to the integration performed by the control loop. The asymptotic value of I_+ is kept constant to the reference laser value acting on RF amplifier gain G.

This feedback has the effect of rejecting minor variations of the cavity laser frequency detuning and mayor variation of losses in the mean value of + light intensity, however we remark that the detuning phenomena is negligible. Intensity loop has also the effect of dropping the dependence of mean I_+ value from the cavity losses of the + traveling wave, and also to modulate the −mono-beam intensity with the + losses low frequency drift, being itself a function of the gain. Empiric observation of I_- proves that the mean value of the mono-beam follow gain dynamic. However I_- is compensated by the gain to a constant value with drifts on the scale time of hours, as losses of each beam have the same magnitude. Gain is an input signal, it can be sampled and acquired with low noise addiction for EKF filtering purpose.

3.4.3   Experimental results of the stabilization loops

We discuss now the two feedback of G-PISA from an experimental point of view. Control signals and error signals of both loops have been acquired for the date of 15/09/2011 ($GPS = 10000000000$). All acquired signals are displayed in units of Volts. The calibration constant of the error signal of the perimeter loop is $\simeq 10^6 Hz/V$ so that the values can be read in MHz. Both correction signals displayed are proportional to the output voltage of the PID controller, and they are scaled with an offset. The intensity loop error signal has been calibrated as discussed in Section 6.

First figure in 3.2 shows the behavior of the two loop corrections on a day of running operations: those signals are corrections of temperature and pressure inducted drift, respectively on ω_+ and μ_+. Third and fourth plots shows the plot of the two loop errors in the selected day. Note that the two errors have approximately null mean, so that the assumption of regime operation for both loops hold. The behavior of the perimeter loop error signal represents ω_+, this signal is self-calibrated thanks to a feedback on the length of the Fabry-Perot scanner. We recorded a maximum detuning + variation of $\Delta\omega_+ \sim 5\ MHz$. The
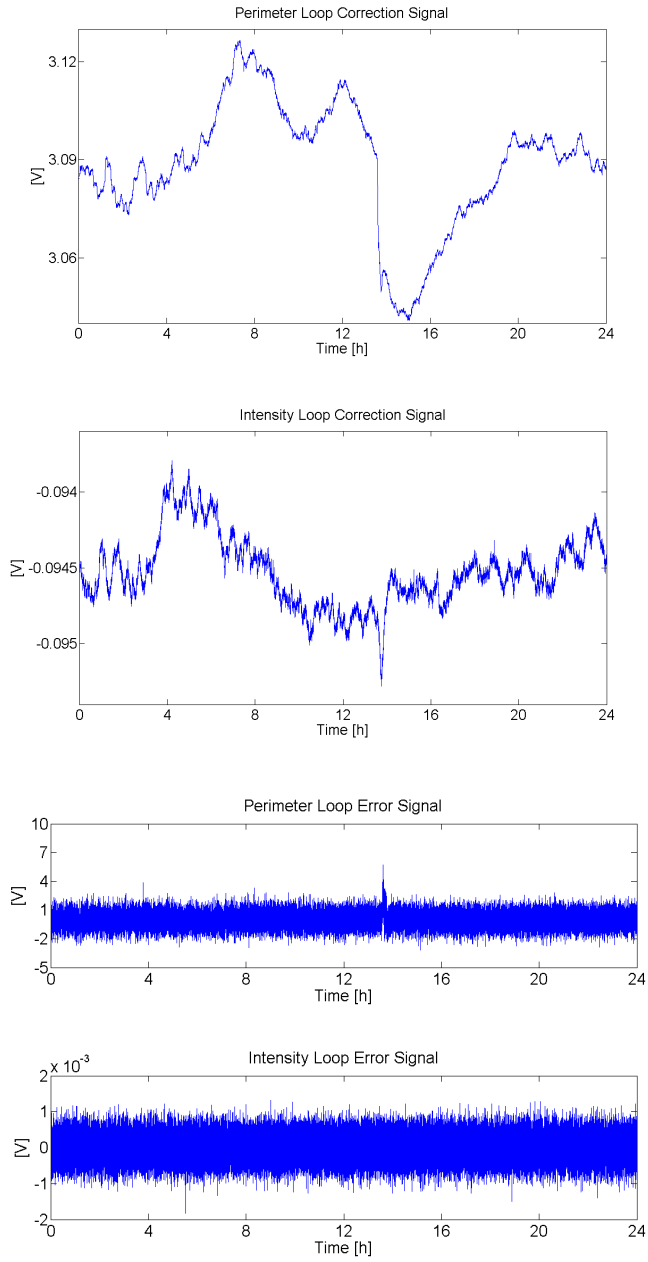
35

Figure 3.2: Plot of one day of loops operations. The first and second plots show the correction signals, the third and the fourth plots show the error signals. In the correction signal detection procedure some data have been lost due to hardware failure. Corrupted data are not displayed.
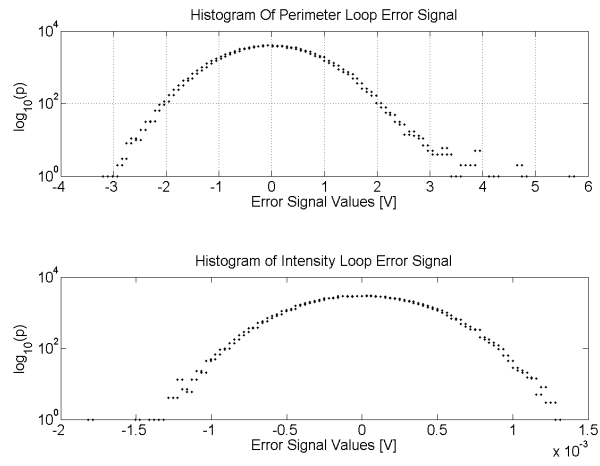
36

Figure 3.3: Histograms of the perimeter and intensity loop errors showing the Gaussian distribution of fluctuations.

behavior of the intensity loop error signal is proportional to $I_+ \propto P_{out}$.

Fig.3.3 displays the histograms of both loop errors. We recognize a parabolic behavior, which correspond to a Gaussian distribution in the logarithmic scale.

4 Identification Routine

To implement EKF routine for the estimate of back-scattering contribution to the Sagnac frequency, scattering parameters $r_\pm$ and ε, gain G, and losses $\mu_\pm$ should be consistently identified. To this aim, we search for relations among the mean intensity values, the oscillating intensity modulation amplitudes and phases and the RLG parameters. Then we describe the numerical implementation of the identification procedure. Unfortunately, the non-linearity of Eqs.(3.3) makes unaffordable any general approach, and the study of this problem must be carried out carefully by inspecting the particular form of RLG equations together with the of G-PISA experimental data.

4.1 Perturbative Fundamental Solutions

As illustrated in Fig.4.2, the Fourier analysis of the acquired data intensities $\{I_\pm(n)\}$ and interferogram $\{S(n)\}$ shows that the fundamental Sagnac harmonic at 107.2 Hz dominates the plots. Moreover, as shown in Fig.4.1, the intensities have an offset. On this offset a sinusoidal component is superimposed at the Sagnac frequency. Therefore we search for solutions of Eqs.(3.3) in the form of a constant plus a sinusoidal signal for the intensities and of a linear growth in time for the phase.

Following ref.[17] its useful to express the intensities and the scattering coefficients in terms of their sum and difference

$$I = \frac{I_- + I_+}{2}, \quad i = \frac{I_- - I_+}{2} \quad ,$$

$$R = \frac{r_- + r_+}{2}, \quad r = \frac{r_- - r_+}{2} \quad ,$$

(4.1)

and normalize all RLG parameters in units of rotation rate by defining

$$\Omega_{a\pm} = \alpha_\pm \cdot \frac{c}{L}, \quad \Omega_b = \beta \cdot \frac{c}{L} \quad ,$$

$$\Omega_R = R \cdot \frac{c}{L}, \quad \Omega_r = r \cdot \frac{c}{L} \quad .$$

(4.2)

We assume $\alpha_+ \simeq \alpha_- \simeq \alpha$, and neglect the terms in i in the equation of I and we consider constants the terms in I in the equation of i. As reported in ref.[17]
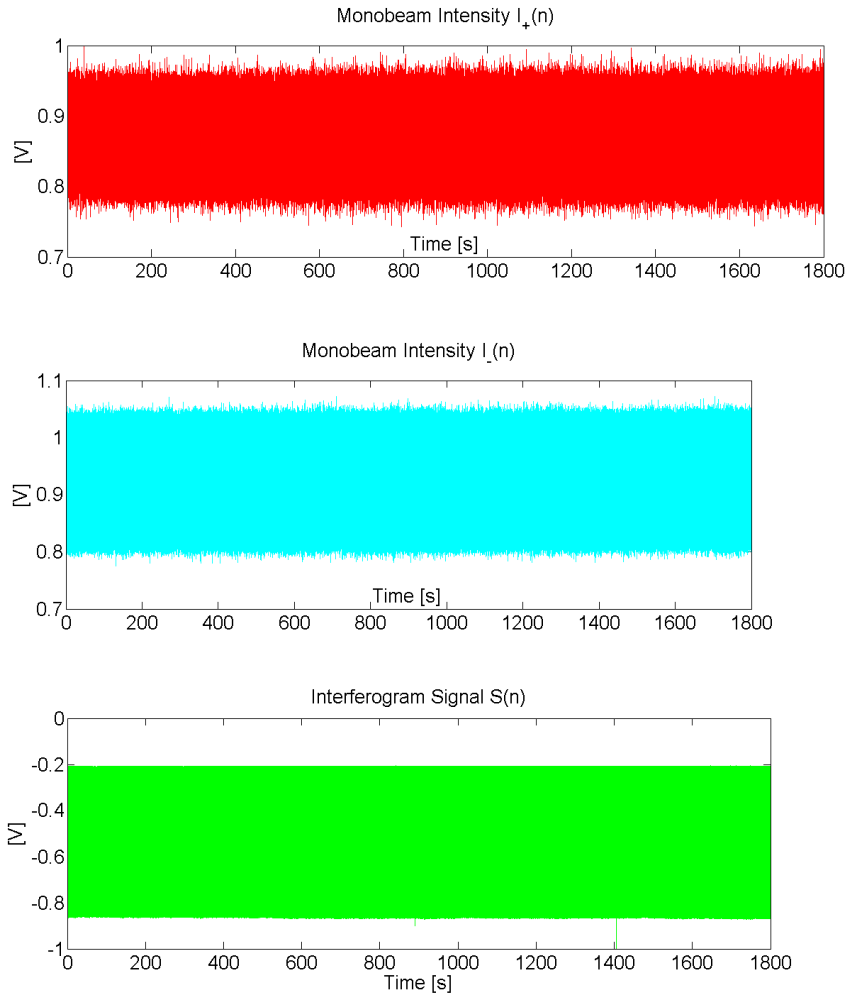
Figure 4.1: Trends of G-PISA main channels during 30 *min* of running operation, time domain. The first plot refers to the un-normalized intensities $\{I_\pm(n)\}$ while the second is the interferogram signal $\{S(n)\}$, as they come from the amplifiers. Note that $\{S(n)\}$ has an bias as well as a scale factor error.
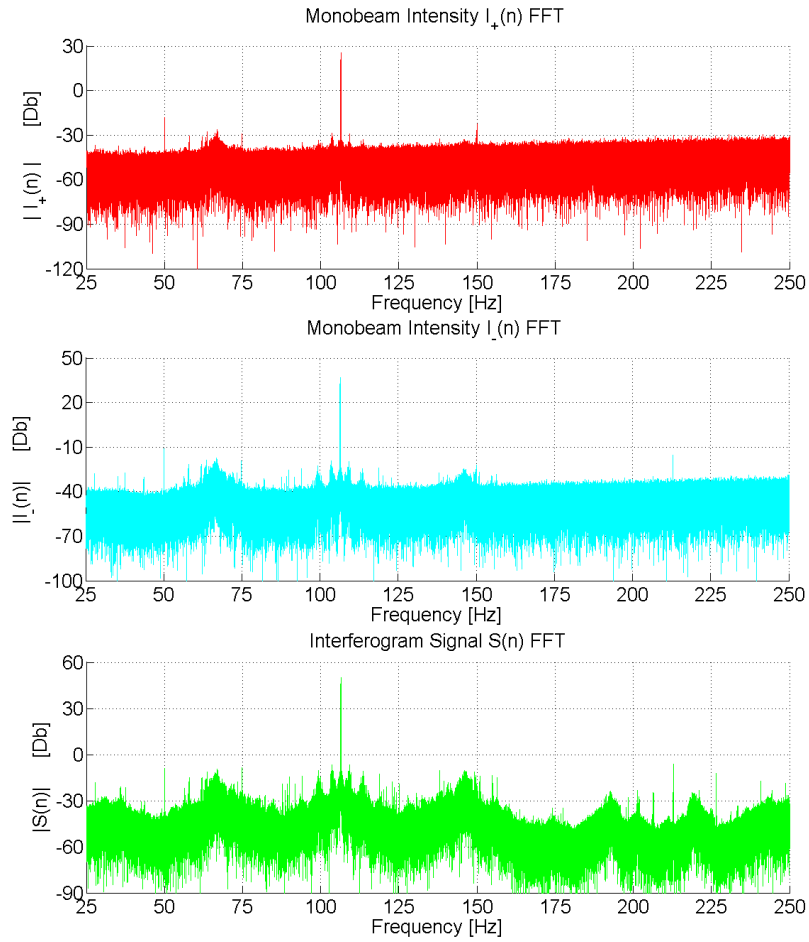
Figure 4.2: Plot of the Discrete Fourier Transform of $\{I_{\pm}(n)\}$ and $\{S(n)\}$ in the Sagnac effect frequency band $(25 - 250)\ Hz$. The first and second plot refers to the intensities while the third is the interferogram signal.

approximate solutions of the new dynamical equations,

$$
\begin{aligned}
\dot{I} &= \Omega_a I - \Omega_b(I^2 + i^2) + 2\sqrt{I^2 - i^2}(A\cos\psi - B\sin\psi) \\
\dot{i} &= \Omega_a i - 2\Omega_b I i + 2\sqrt{I^2 - i^2}(a\cos\psi - b\sin\psi)
\end{aligned}
\tag{4.3}
$$

reads

$$
\begin{aligned}
I &= I_0 + I_1 \sin\Phi_+ \\
i &= i_1 \sin\Phi_- \\
\tilde{\psi} &= \tilde{\omega}t \quad ,
\end{aligned}
\tag{4.4}
$$

where $I_0 = \Omega_a/\Omega_b$, $A = \Omega_R \cos\varepsilon$, $B = \Omega_r \sin\varepsilon$, $a = \Omega_R \sin\varepsilon$, $b = \Omega_r \cos\varepsilon$.

$$
I_1 = 2I_0 \cdot \sqrt{\frac{\Omega_R^2 \cos^2\varepsilon + \Omega_r^2 \sin^2\varepsilon}{\omega_s^2 + \Omega_a^2}},
$$

$$
\tag{4.5}
$$

$$
i_1 = 2I_0 \cdot \sqrt{\frac{\Omega_R^2 \sin^2\varepsilon + \Omega_r^2 \cos^2\varepsilon}{\omega_s^2 + \Omega_a^2}}.
$$

Here, $\Phi_\pm = \tilde{\omega}t + \phi_{0\pm}$ are phases of the mono-beam oscillating parts, and $\tilde{\omega}$ is the Sagnac pulsation pulled or pushed by scattering effects. Its worth noticing that the previous considerations still holds at first approximation if $\alpha_+ \neq \alpha_-$ and one considers I and i as a convex combination of laser mono-beam intensities that provides a null offset to i, i.e.

$$
I = w_+ I_+ + w_- I_- \quad , i = w_+ I_+ - w_- I_- \quad ,
\tag{4.6}
$$

where

$$
w_+ = \frac{\alpha_-}{\alpha_+ + \alpha_-} \qquad w_- = \frac{\alpha_+}{\alpha_+ + \alpha_-}
\tag{4.7}
$$

Then the normalized parameters become

$$
\Omega_a = \frac{\alpha_+ + \alpha_-}{2} \cdot \frac{c}{L}, \qquad \Omega_b = \beta \cdot \frac{w_+ + w_-}{4w_+ w_-} \cdot \frac{c}{L}
$$

$$
\tag{4.8}
$$

$$
\Omega_R = \frac{r_- w_+ + r_+ w_-}{2\sqrt{w_+ w_-}} \cdot \frac{c}{L}, \quad \Omega_r = \frac{r_- w_+ - r_+ w_-}{2\sqrt{w_+ w_-}} \cdot \frac{c}{L} \quad ,
$$

41

Within these approximations, the identification procedure can be split into two parts:

i)   Retrieve the losses values from the offset of the intensities and from the acquired signal of the gain.

ii)   Use the oscillating part of the intensities to identify both scattering coefficients $r_\pm$ and angle ε.

4.2   Losses Identification

To identify losses we write the mean light intensities $I_\pm$ as

$$< I_\pm > = \frac{\alpha_\pm}{\beta} \quad , \tag{4.9}$$

here we use the notation $< x >= \sum_{n=1}^{N} x(n)/N$ to denote mathematical expectation as Eqs.(3.3) describe an ergodic system.

We explicit the losses and gain dependence on $\alpha_\pm$, and β

$$\frac{G - \mu_+}{G} = < I_+ > , \qquad \frac{G - \mu_-}{G} = < I_- > \quad . \tag{4.10}$$

Therefore we have

$$\mu_\pm = (1- < I_\pm >)G. \tag{4.11}$$

Following this approach one can estimate losses by averaging $I_\pm$ during a time period that corresponds to many Sagnac phase cycles, but with negligible losses variation.

4.3   Identification of the Scattering Angle

To identify the scattering angle ε we further discuss the back-scatter geometrical approach described in Section 3: a part of one light beam phasor is added in opposition to the other, therefore the phase $\Phi_\pm$ of both beams oscillating part is pulled or pushed, on average, by ε.

$$\Phi_+ \simeq \psi + \varepsilon, \ \Phi_- \simeq \psi - \varepsilon \qquad . \tag{4.12}$$

From the average estimation of phases of both oscillating intensity contributions $< \Phi_\pm >$, we can identify the scattering angle as

$$\varepsilon = \frac{< \Phi_+ > - < \Phi_- >}{2} \qquad . \tag{4.13}$$

4.4 Identification of the Scattering Coefficients

To identify scattering coefficients $r_\pm$ we invert the relations of Eq.(4.5) and make use of the values of $\mu_\pm$ and ε, previously identified.

$$\begin{bmatrix} \Omega_R^2 \\ \Omega_r^2 \end{bmatrix} = \frac{\omega_s^2 + \Omega_a^2}{2I_0 cos\, 2\varepsilon} \cdot \begin{bmatrix} cos^2\varepsilon & -sin^2\varepsilon \\ -sin^2\varepsilon & cos^2\varepsilon \end{bmatrix} \cdot \begin{bmatrix} I_1^2 \\ i_1^2 \end{bmatrix} \tag{4.14}$$

However, some ambiguities arise in the solution for $r_\pm$, since these equations do not provide a criteria to find the greatest of the two scattering coefficients. We note that in Eqs.(3.3) the parameters $r_\pm$ directly affect $I_\mp$. Therefore we identify the subscript of $max\{r_\pm\}$ with the subscript of the minimum root mean square of the acquired intensity.

As done in the previous sections, we estimate $< I_1 >$ and $<i_1 >$ for a time period where both modulations have a constant amplitude. Using Eq.(4.14) and the suitable sign s the scattering coefficients can be identified as $r_\pm = \Omega_R \pm s \cdot \Omega_r$.

4.5 Data Conditioning for Identification Procedure

To complete the identification procedure we give the estimation we devised for the quantities $< I_\pm >$, $< I_1 >$, $< i_1 >$, $< \Phi_\pm >$. The identification results will be discussed later in Section 6.

Firstly we address to the estimation of the mean mono-beam part. The straight forward approach is to average over time $I_\pm$, so that both oscillating signal and noise contributions are asymptotically removed from the mean value. However, losses induces drifts on $I_\pm$, so that the average procedure must be stopped and iterated after some time. The time interval of the average must be chosen

43

according to oscillation and noise rejection, and the time scales of drifts, and also accounting intensity feedback action. Intensities signals are firstly decimated by a factor of 8 and low pass filtered with a 1st order Butterworth filter, to smooth oscillating parts. then $I_{\pm}$ are averaged on different time intervals $10 \div 100 \ s$.

The decimation procedure has been carried out with Zoom and Decimation of a factor 2^n (ZD n), a tail recursive routine which iteration step is:

i)   an half band filter stage with transfer function

$$H(z) = \frac{z^3 + 2z^2 + 2z + 2}{4z^3 + 2z}$$

ii)   a down sample by a factor of 2.

This procedure ensure a linear phase filter response with $n = 3$ iterations, thus avoiding phase distortion of the filtered signals.

The phase estimation of the two mono-beam oscillating parts is carried out using the Discrete Hilbert Transform. We remark that uncertainty usually arises while trying to estimate both the amplitude and the phase of a noisy sinusoidal signal. Assumptions on the quantity corrupted by noise (phase or amplitude) are necessary in this case. On the one hand Hilbert transform suppose that all noise in the sinusoidal time series is phase noise, and it is suitable on phase estimate. On the other hand Lock-in procedure makes the opposite assumption and it is preferred when one is interested in amplitude estimates.

Intensities signal acquired at $5 \ kHz$ are decimated by a factor 2 with ZD 1 and band passed around the Sagnac band $[95 \div 125] \ Hz$ by mean of a Butterworth filter, in order to reject frequency contributions different from the first Sagnac harmonic. The Hilbert transform of the conditioned time series is computed. Finally the phase difference of the mono-beam light intensity is estimated with an average operation on the unwrapped phase angle difference, retrieved using arctan($\cdot$) Matlab function.

A digital lock-in estimates the amplitudes of oscillating mono-beam parts. Firstly I, i and S are decimated and bandpass filtered as in the previous case. The Hilbert transform of the phase difference is computed to get the in-phase and in-quadrature parts of the Lock-in signal, then the sum and the difference of the light intensities are demodulated via time domain multiplication and low pass
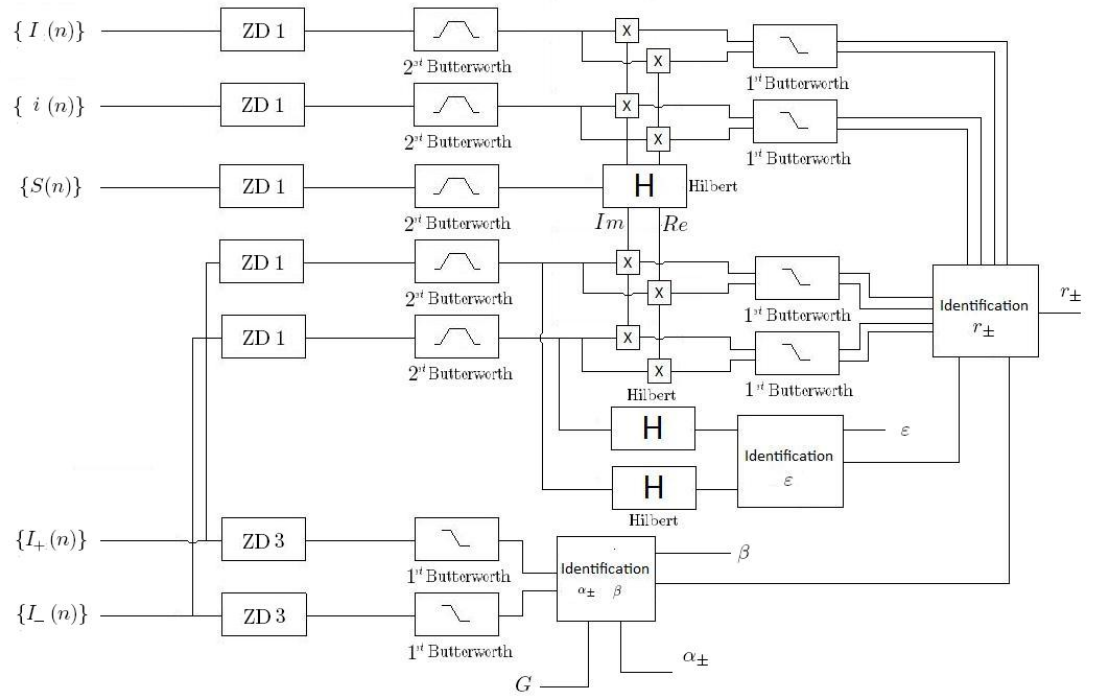
44

Identification Scheme

Figure 4.3: Schematic of the identification procedure.

filtering. Its worth noticing that, using the phase difference as demodulating carrier, the digital Lock-in is robust to phase out and parameters time-variation.

The identification scheme is sketched in Fig.4.3.

5   EKF implementation

We address now to the implementation of the extended Kalman filter. We follow the approach discussed in ref.[5] and use the same notation.

5.1 EKF Model

The EKF model we devise for the estimate of the rotation signals is based on Eq.(3.3), with the approximations discussed in Section 3 ($\theta_{\pm,\mp} = 0$, $\tau_{\pm,\mp} = 0$, $\sigma_{\pm} = 0$). Since the identification procedure has been carried out for the RLG parameters $\mu_{\pm}$, $r_{\pm}$, ε, their value is assumed known, so that the EKF state variables are $\mathbf{x} \in \mathbb{R}^3$, $\quad \mathbf{x} = [x_1 \ x_2 \ x_3]^T = [I_+ \ I_- \ \psi]^T$. The EKF prediction step which corresponds to the integration of Eqs.(3.3) over the sample time interval is carried out using the RK4 routine. The EKF equation model is $\dot{\mathbf{x}} = \mathbf{F}(\mathbf{x}, t) + \mathbf{v}(t)$. The error model $\{\mathbf{v}(t) \in \mathbb{R}^3, \ t \in \mathbb{R}\}$ is the sum of several contributions:

i)　　　　RK4 integration Error on the Sample time interval

ii)　　　　detuning frequencies effect that has been disregarded

iii)　　　　identification error on $\mu_{\pm}$, $r_{\pm}$ and ε.

iv)　　　　Errors due to the physical approximations used to derive the laser dynamics described by Eqs.(3.2).

We point out that also the noise on the acquired signal G contribute to the identification error. However, the main contribution to model error process is due to identification errors, and we can approximate the sum of these error processes with it. Since the magnitude of the resulting process is small, we get an estimation of the magnitude of its 2nd moment matrix Q approximating the error process as a stochastic Markovian process [5].

The observation model provided is $\mathbf{y} = [y_1 \ y_2 \ y_3]^T = [x_1 \ x_2 \ sin(x_3)]^T + \mathbf{w}^T(t)$. The three detectors introduce additive noise, and the sinusoidal signal of phase difference is affected by optical misalignment and loss of contrast. The measure error $\{\mathbf{w}(t) \in \mathbb{R}^3, \ t \in \mathbb{Z}^+\}$ is then made of two contributions:

i)　　　　additive noise of the photo detector (current fluctuations at the input of the amplifiers)

ii)　　　　bias and scale error of the interferogram signal

Since $S(n)$ is affected by loss of contrast and optical misalignment, which results in a bias and in a scale factor error, to recover a good sinusoidal signal for the

46

phase difference we remove the linear trend in y_3 and normalize it for twice its variance. This procedure deletes the second error source mentioned, but it introduces another error source in $\mathbf{w}(t)$. However, this last source is of small magnitude if compared to measure error, and can be neglected. Therefore the 2^{nd}moment matrix of $\mathbf{w}(t)$ can be approximated considering only the detector additive noise.

5.2   EKF Matrices

In this subsection we discuss the choice of the EKF matrices Q and R. By definition the matrix Q is the variance of the continuous time noise vector process $\mathbf{v}(t)$ that affects EKF state [5]. We model this error process with the identified parameters error effect on the EKF state. Defining the identified parameters vector as $\hat{\mathbf{k}} = [\hat{\mu}_\pm \ \hat{r}_\pm \hat{\varepsilon}]^T$ we get

$$\dot{\mathbf{x}}(t) \;=\; \mathbf{F}(\hat{\mathbf{x}}, \hat{\mathbf{k}}) \;+\; \mathbf{v}(t) \qquad . \tag{5.1}$$

Considerations of Section 6 on the identification errors magnitude and Eqs.(3.3) form emphasize the role of the identification error of $r_\pm$ in the $\psi(t)$ dynamic, and show that in the $I_\pm$ dynamic error contribution related to $r_\pm$ and $\mu_\pm$ are of the same magnitude. Neglecting thus ε identification error contribution $\mathbf{v}(t)$ can be approximated as

$$\begin{cases} v_1 & \sim N(0, \ \sigma_1^2) \\ v_2 & \sim N(0, \ \sigma_2^2) \\ v_3 & \sim N(0, \ \sigma_3^2) \end{cases} \tag{5.2}$$

where

$$\begin{cases} \sigma_1 \sim & \delta r_- < \sqrt{I_+ I_-} > +\delta\alpha_+ < I_+ > \\ \sigma_2 \sim & \delta r_+ < \sqrt{I_+ I_-} > +\delta\alpha_- < I_- > \\ \sigma_3 \sim & \delta r_+ < \sqrt{I_+/I_-} > +\delta r_- < \sqrt{I_-/I_+} > \end{cases} \qquad , \tag{5.3}$$

here $\delta r_\pm \;=\; \sqrt{< c/L(\hat{r}_\pm - r_\pm)^2 >}$ and $\delta r_\pm \;=\; \sqrt{< c/L(\hat{\alpha}_\pm - \alpha_\pm)^2 >}$ If we assume that the errors in $+$ and $-$terms are equal, since intensities are of the

same magnitude, and consider equal the error on the $\pm$ scattering coefficients and on losses we get

$$\begin{cases} \sigma_1 & \sim (\delta r + \delta\alpha) < I > \\ \sigma_2 & \sim (\delta r + \delta\alpha) < I > \\ \sigma_3 & \sim 2\delta r \end{cases} \qquad . \qquad (5.4)$$

The last point is to provide the correlations between the components of $\mathbf{v}(t)$. To this aim we assume no correlation on the components v_i, and the matrix Q will be of the form of

$$\begin{bmatrix} \sigma_1^2 & 0 & 0 \\ 0 & \sigma_2^2 & 0 \\ 0 & 0 & \sigma_3^2 \end{bmatrix} \qquad . \qquad (5.5)$$

The determination of the R matrix is simple as the measure noise is dominated by photo detectors additive noise, which is Markovian and Gaussian distributed. Since the detectors are not plugged to the same generators and they are displaced at different points of the G-PISA structure we assume no correlations between the components of $\mathbf{w}(t)$. Therefore R is a diagonal matrix. The scalar variance of each component of the diagonal of R can be estimated with detectors data sheets and considerations on the Fourier transform of the experimental signals.

5.3 Frequency Detection

After the application of the EKF, the Sagnac frequency must be estimated. To this purpose we estimate ω_{BS} using the filtered channels $\hat{I}_\pm$, $\hat{\psi}$ and Eq.(3.4), and we compute the numerical derivative of $\hat{\psi}$ by using its discrete approximation, called 5 point method, that ensure a good noise rejection and accuracy.

$$\dot{\hat{\psi}}(k) = \frac{\hat{\psi}(k-2) - 8\hat{\psi}(k-1) + 8\hat{\psi}(k+1) - \hat{\psi}(k+2)}{12\Delta t} \qquad , \qquad (5.6)$$

where Δt is the sampling time. This method generates an approximation error bounded by $\dfrac{\Delta t^4}{30} U$, where U is the maximum value of the 5th derivative of ψ in the sampling interval.

The estimated Sagnac frequency in the discrete time domain reads

$$\hat{f}_s(k) = \frac{\dot{\hat{\psi}}(k) - \hat{\omega}_{BS}(k)}{2\pi} \qquad .$$

After the cancellation of the back-scattering dynamics, $\hat{f}_s(k)$ can be converted in physical rotation rate by means of the scale factor $SF = \lambda L/4A$. Its worth noticing that the band of the rotation signal for an Earth based RLG is $\sim 1\ Hz$ and then $\hat{f}_s(k)$ can be decimated by a huge factor (e.g. 1000).

6 Results and Discussions

In this Section we discuss some results we obtained from simulated and experimental data concerning the identification and the frequency estimation.

6.1 Simulation Model

The numerical simulation of RLG dynamics is of paramount importance for debugging software, for the identification procedure and the correct implementation of the Kalman filter. We describe now the simulation we have implemented.

Eqs.(3.3) have been numerical integrated by using RK4 procedure. The RLG parameters have been chosen according to Tab.(3.2). We then focused attention our on feedback effects on RLG parameters. In Section 3 we showed that both control loops introduce very slow parameter variations in Eqs.(3.3). Therefore no dynamics of parameters are accounted for in the simulation routine. Moreover, we suppose stationary working conditions for both control loops.

To simulate the perimeter loop dynamics we model losses and scattering parameters as random walk drifts at $1\ Hz$ frequency on their reference values. These random walk processes are simulated assuming a small perturbation of their reference value. Typically we use a standard deviation $10^{-1} \div 10^{-3}$ times the parameter value and a time correlations $\sim 10\ min$. These features are much worse than the experimental data of G-PISA. However, the results of such simulations should put in evidence any critical point of the implemented procedures.

To simulate the intensity loop dynamics, we change the gain value in each second of simulation second to keep constant the ratio $(G - \mu_+)/G$. Thus the gain will follow μ_+ dynamic rejecting at the same time the fluctuations of the mean level of I_+.

Fig. 6.1 shows the results of 10 min of simulation. The Tab.6.1 shows the utilized parameters; to simulate the dissipative coupling, the initial value of ε is set to 0, and the simulation sampling rate is 5 KHz as in the G-PISA experiment.

The simulation results are shown in Fig.6.1. As expected from analysis in Section 3, the mono-beam intensities have a mean value with a small a.c. modulation superimposed. In the second plot we display the time derivative function

Parameter	$+$		$-$
α	$1.35 \cdot 10^{-8}$		$1.35 \cdot 10^{-8}$
β		$1.0135 \cdot 10^{-6}$	
ω_s		$107.2 \cdot 2\pi$	
r	$2 \cdot 10^{-7}$		$2 \cdot 10^{-7}$
ε		0	

Table 6.1: Reference values of RLG parameters close to the typical values of G-PISA that have been chosen.

of the phase difference $\dot{\psi}$ normalized from pulsation to frequency. $\dot{\psi}$ varies from 104 to 111 Hz, and this is due to back-scattering contributions ω_{BS} in Eqs.(3.3).

6.2   RK4 integration error

To estimate RK-4 integration error, we calculated the closed form solutions of Eq.3.17, and compared with its numerical integration. To this purpose we get an RLG parameters set consistent with the assumptions made in case of symmetric scattering: in particular we set the $'-'$ values equal to the corresponding $'+'$ values. With these parameters the intensity ratio of the simulated $I_\pm$ is shown by Matlab to be exactly 1, so the approximations made in Eq.(3.17) holds.

Fig. 6.2 shows the results of computation. Firstly we point out that the two numeric integrated equation slightly differ from the analytic solution while the two numerically integrated phases do not sensibly differ, as Matlab returned the null function after we computed their difference. After half an hour of simulation the difference between the two curves is small. Fig.6.3 displays the relative integration errors. The error growth versus time is in agreement with stiff equations theory. We note that the two error are of the same magnitude and that their final absolute value is of the order of 10^{-4}. Therefore a simulation of 30 min seems to describe with good approximation the RLG dynamic, as the integration error maximum modulus is under the level of the detection noise.

6.3   Identification Tests

Here we present a summary of the tests made on the identification procedure. The variation of all parameters are 10^{-2} times their reference value of Tab.6.1. Fig.6.3 shows the relevant parameters for the simulated RLG dynamics: α_+ is
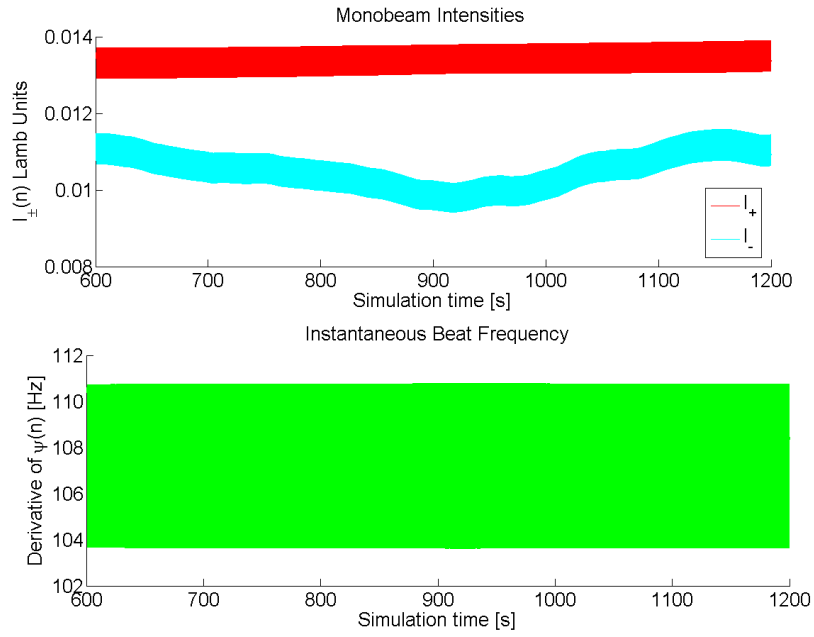
Figure 6.1: Simulated version of RLG dynamic for 10 minutes of running operations. The plots show the light mono-beam intensities $I_\pm$, and the instantaneous beat frequency, respectively.
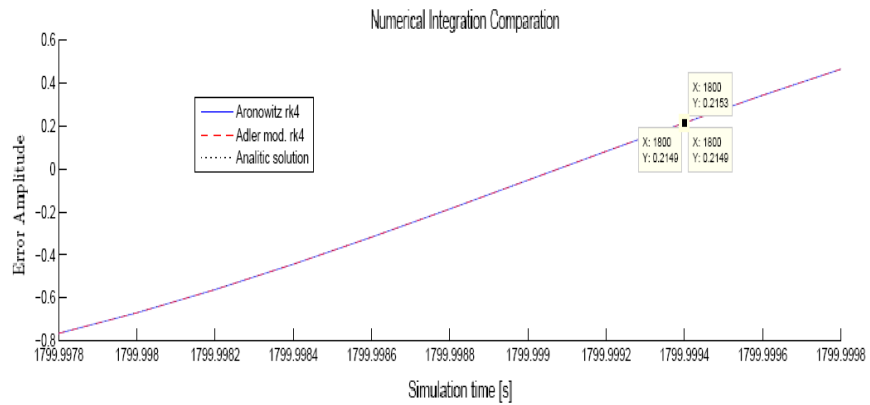

Figure 6.2: The simulated trend of interferogram signal $\{S(n)\}$: Eq.(3.3) in blue; Eq.(3.14) in red; and Eq.(3.17) (analytic solution) in black. Simulation time is 30 min, and step size is $5 \cdot 10^{-3}$ s. Only the last 10 samples are displayed.
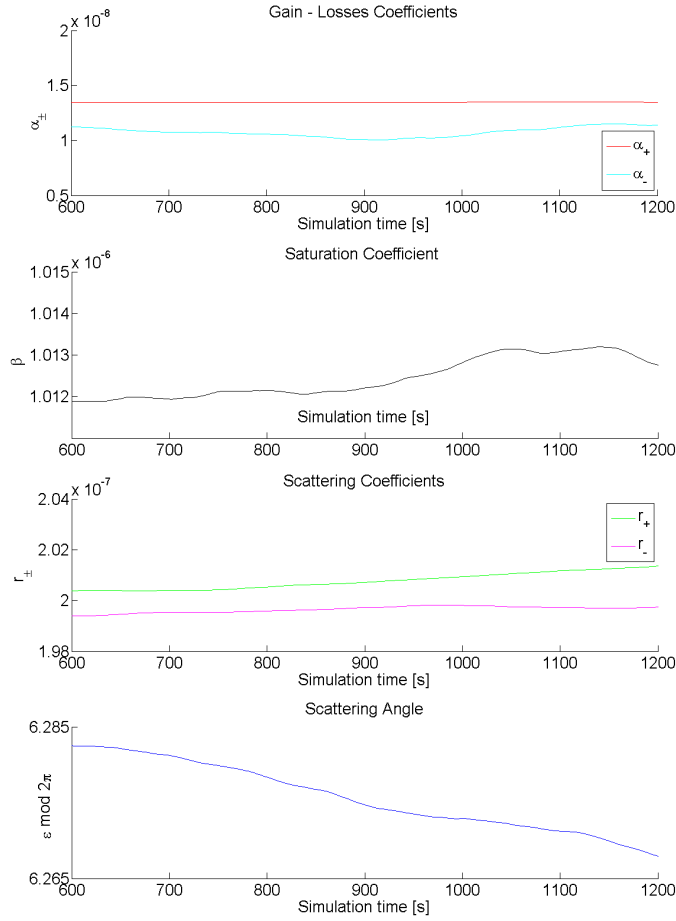
Figure 6.3: Simulated RLG parameters during 10 min. The resulting intensities and instantaneous frequency are displayed in Fig.4.3.

affected by intensity loop, and the changes of β are determined by the drift of μ_+ because of the loop action.

6.3.1 Logistic Parameters

In Fig.6.4, the trends of the continuous parts of $I_\pm$ is compared with the excess gain minus losses over the gain ratios $\alpha_\pm/\beta$; we show the moving average on $1\ s$ time interval for all signals. Simulation runs with different RLG parameters show that α_+/β and α_-/β are in correlation. We note that in the final part of the plot the intensities mean value slightly differs from the ratios $\alpha_\pm/\beta$.

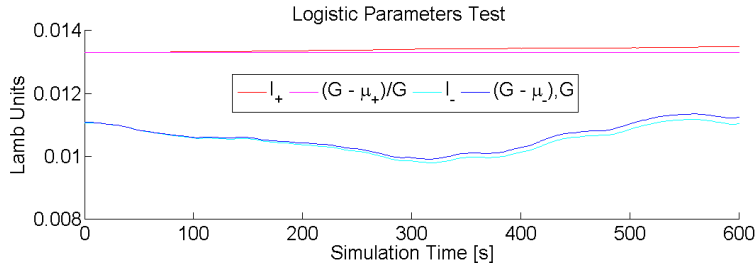Figure 6.4: Comparison between the continuous part of intensities and the $\alpha_\pm/\beta$ ratios.
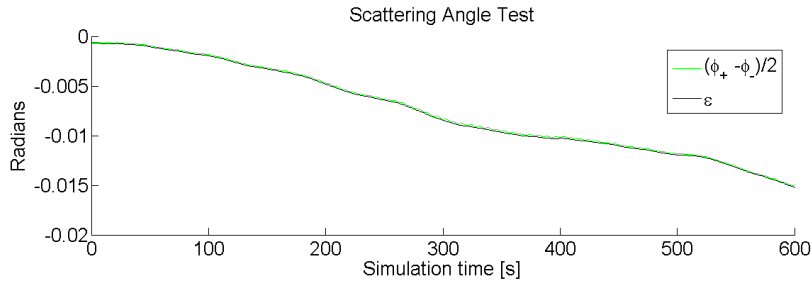

Figure 6.5: Plots of scattering angle ε behavior compared to the observable given in Section 4.

The simulations show that in presence of different scattering coefficients the identification of the logistic parameters presents a small bias. Therefore the continuous intensity parts are not exactly determined by the logistic parameters and the loss estimates independently form scattering coefficients are biased.

6.3.2   Scattering Angle

To test the identification procedure of the scattering angle we compare the simulated behavior of ε with the observable $(\Phi_+ - \Phi_-)/2$. We retrieve the oscillating parts from the simulated $I_\pm$ and use the Hilbert transform to get the phases. Finally, we compute the moving average on $1\ s$ time interval for both signals. Fig.6.5 shows the comparison. We note that there is a good correlation between the scattering angle and $(\Phi_+ - \Phi_-)/2$; nevertheless a small constant bias is still present. We note that the scattering angle estimation can be carried out independently of the other parameters.

54

6.3.3 Scattering Coefficients

To discuss the identification procedure of the scattering coefficients we compare the modulations of the convex intensity combinations of Eq.(4.6) with Ω_R^2 and Ω_r^2 exploiting relation (4.5). We combine together the simulated light intensity signals as prescribed by Eq.(4.5), then we use a digital lock-in to estimate the modulations of I and i. The digital lock-in requires the calculation of both the "in phase" ($\cos\psi$) and "in quadrature"($\sin\psi$) of the carrier. As the interferogram signal only provides the $\sin\psi$ component (stated definition), $\cos\psi$ has been estimated by means of the Discrete Hilbert Transform. In Fig.6.6 summarizes the results; in both graphs the simulated and identified intensities I_1 and i_1 differs, and simulations indicate that this bias is related to asymmetric losses $\mu_+ - \mu_-$.

6.4 Identification of Simulated Parameters

The identification routine has been implemented exploiting the overlap and save method. Each identification step involves 30 min of simulated data, the time series of $\{I_\pm(n)\}$ and $\{S(n)\}$ are divided into three data blocks labeled as "past" $(0 \div 10\ min)$, "present" $(10 \div 20\ min)$ and "future" $(20 \div 30\ min)$. All data blocks are gathered together and processed to estimate $< I_\pm >$, $< \phi_\pm >$, $< I >$ and $< i >$. Firstly $\{I_\pm(n)\}$ are decimated by a factor 8 with ZD 3 and low-pass filtered by means of a Butterworth 1st order low-pass filter with cutoff frequency of 1 Hz. The output is then averaged for each second of simulation on 10 s of values for I_- and on 100 s for I_+, as I_- variations are faster than I_+. Then $\{I_\pm(n)\}$ time series are down-sampled by a factor 2 with the use of the recursive filter, the output is bandpass filtered by mean of a 2nd order Butterworth filter with band of [95, 125] Hz. The complex phase of the discrete Hilbert transforms of the outputs is averaged for each second of simulation on 10 seconds of values. Finally the original signals of I, i, S are decimated of a factor 2 and band filtered. $\{I_\pm(n)\}$ and $\{S(n)\}$ are demodulated with the usual digital lock-in and smoothed with a moving average of 1 s. Only the "present" data blocks of all time series are involved in the moving average, thus neglecting the effect of the boundaries due to Discrete Fourier Transform and / or digital filters initial conditions. The parameters $\mu_\pm$ are identified with the use of G values and Eq.(4.11) , ε is identified with Eq.(4.13), and $r_\pm$ are identified using Eq.(4.14) and the other identified parameters, with the convention that $r_+ > r_-$
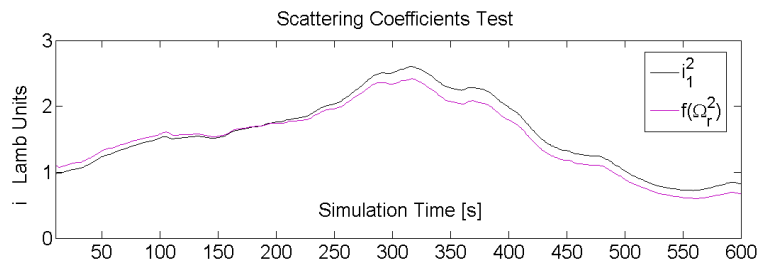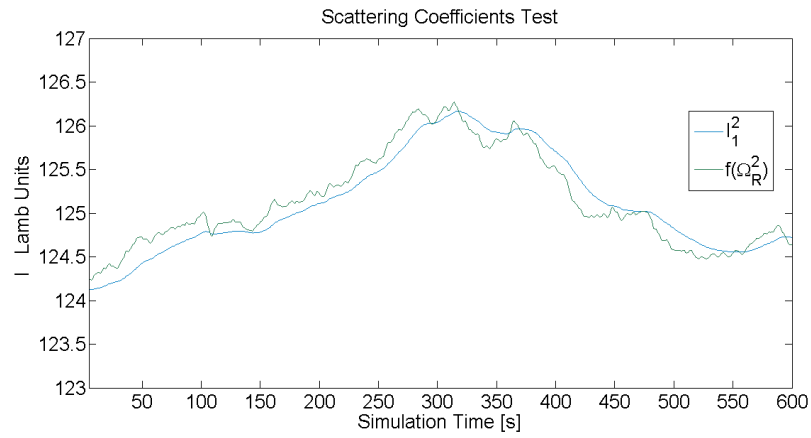
Figure 6.6: Plots of I, i intensities amplitude modulations compared to the analytical expressions given. The upper plot refers to I, the lower plot refers to i.
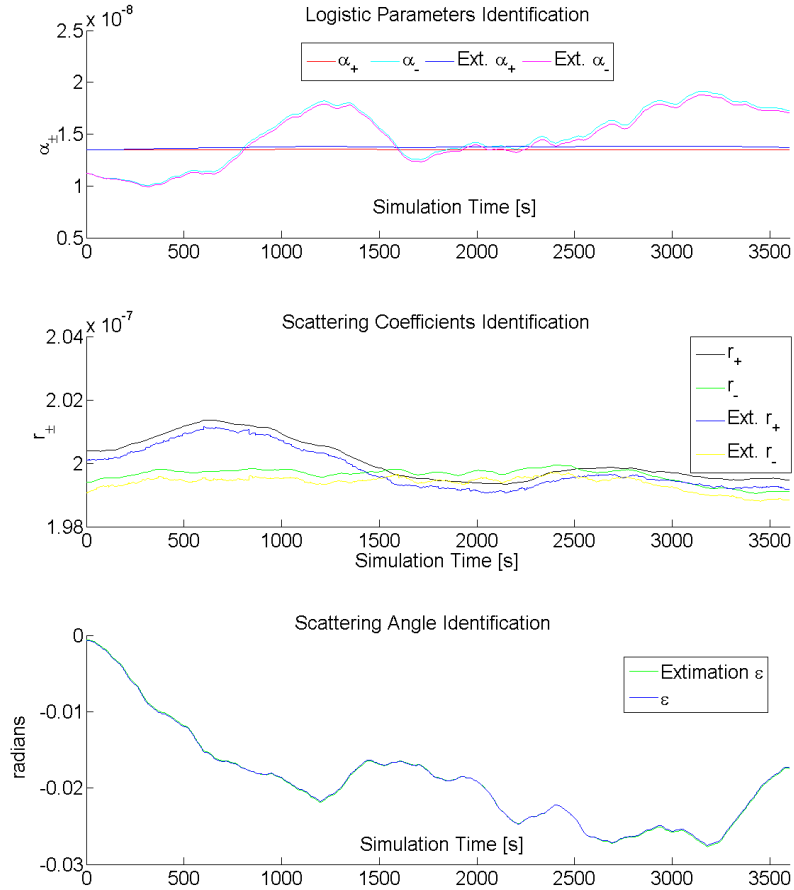
Figure 6.7: Results of the Identification routine for 80 *min* of simulated data. The plots display the comparison between the identified and true parameters.

if $var\{I_-(n)\} > var\{I_+(n)\}$. After the accomplishment of the identification operations the time index of the last data involved is shifted of 10 *min* on the left: so a new data block is now labeled as "future", "future" data block become "present", "present" become "past", and "past" data block is discarded.

The identification routine has been tested on 80 *min* of simulated data. The parameters reference values are given in Tab.6.1. Fig.6.7 shows the results. Each of the three identification estimators is affected by systematic error. Absolute errors on $\alpha_\pm$ and on ε have a drifting bias and small fluctuations. The relative error on the losses, on the scattering angle and on the scattering coefficients is of the magnitude of 10^{-2}, 10^{-3} and 10^{-4}, respectively.
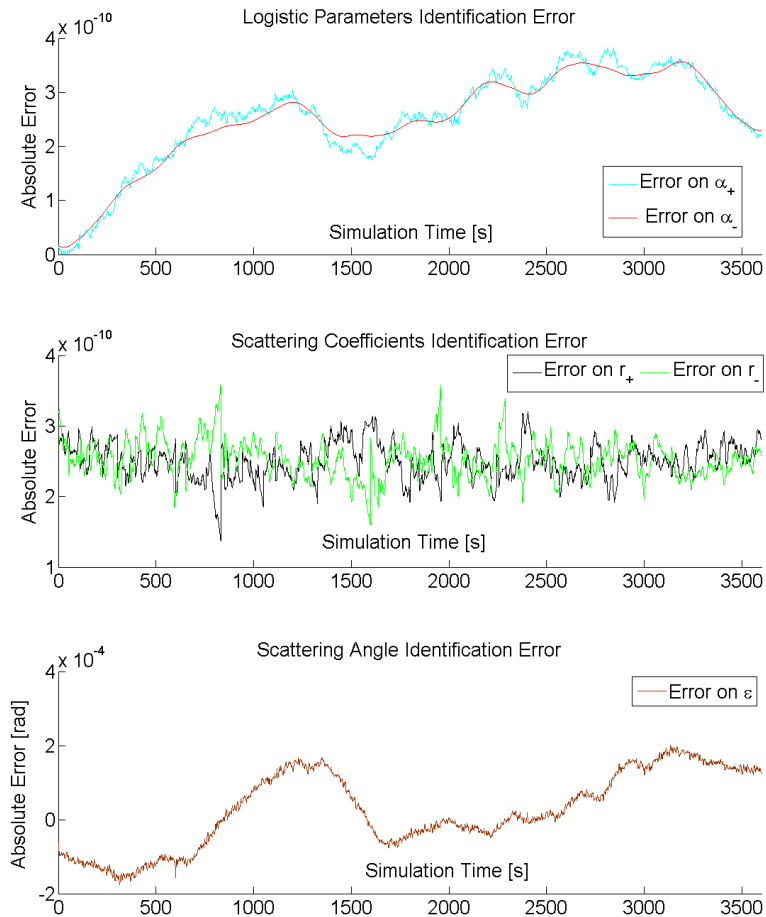
Figure 6.7: Results of the Identification routine for 80 *min* of simulated data. The plots display the absolute error on the identified parameters.

6.5 Frequency Estimation of Simulated RLG Signals

In this Section we report on the simulation results for the frequency estimation using EKF filter. The EKF model presented in Section 5 has been tested on simulated data previously processed by the identification routine. Measure noise has been added to the simulated data, to mimic the actual experiment. The EKF matrices Q (model error covariance) and R (measure error covariance) read:

$$
Q = \begin{bmatrix} 10^{-11} & 0 & 0 \\ 0 & 10^{-10} & 0 \\ 0 & 0 & 10^{-8} \end{bmatrix} \qquad R = \begin{bmatrix} 10^{-4} & 0 & 0 \\ 0 & 10^{-4} & 0 \\ 0 & 0 & 10^{-6} \end{bmatrix} .
$$

On each second of simulation the parameter values are changed in the EKF model as prescribed by the identification routine. The initial conditions of EKF have been chosen as:

i) *State initial value* $x_{0|-1} = [I_+(0), I_-(0), 0]^T$.

ii) *Error matrix initial value* $P_{0|-1} = \begin{bmatrix} 10^{-1} & 0 & 0 \\ 0 & 10^{-1} & 0 \\ 0 & 0 & 10^{-1} \end{bmatrix}$

In Fig.6.8 we report the results. We address to the errors on the EKF state quantities. All three absolute error displayed have a small bias and a dominating fluctuating part. Both absolute errors on the Lamb intensities are $\sim 10^{-5}$, absolute error on the phase is $\sim 10^{-4}$ rad. The small bias affecting each estimation is mainly caused by identification error on $r_\pm$ and $\mu_\pm$. The error on the estimated frequency is decimated at the frequency of $1\ Hz$ by mean of a moving average, it shows a dominating bias part with small fluctuations. The relative error on the Sagnac frequency is one part of 10^{-5} with a bias of 10^{-4} due to the identification errors of the RLG parameters.

In order to determine if EKF is able to track a frequency signal that vary in time, we simulate the RLG dynamic for $1\ h$ adding a small low frequency drift to ω_s, we also add a small asymmetric scattering. RLG parameters are depicted in Tab.6.2. Fig.6.9 shows the results.
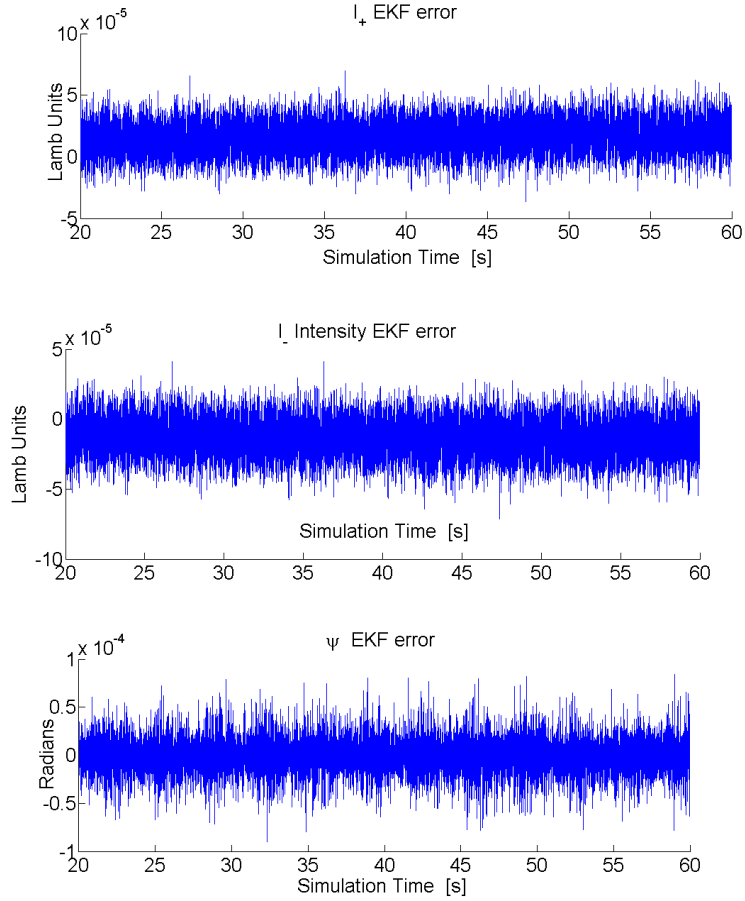
Figure 6.8: Results of frequency estimation. Parameters reference values are displayed in Tab.6.1. Parameter variations are of the order of 10^{-2} on the Hertz scale. The Plots display the three estimation errors in $10\ min$ of operation. Last plot shows the detected frequency error for $1\ h$ of simulated and identified data, at the rate of $1\ Hz$. In this simulation the Sagnac frequency f_s is set constant.

Parameter	$+$		$-$
α	$1.35 \cdot 10^{-8}$		$1.35 \cdot 10^{-8}$
β		$1.0135 \cdot 10^{-6}$	
ω_s		$107.2 \cdot 2\pi$	
r	$2.1 \cdot 10^{-7}$		$1.9 \cdot 10^{-7}$
ε		0	

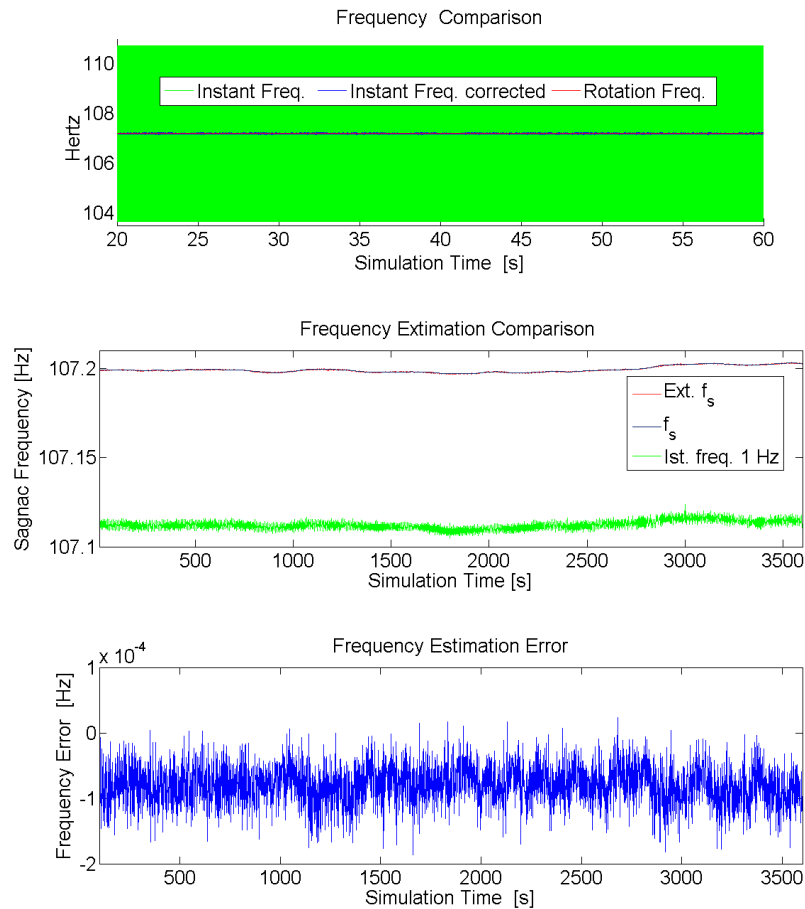Table 6.2: Parameters reference values.

Figure 6.9: Results of frequency estimation. Parameters reference values are the ones of Tab.6.1, all variations are $\sim 10^{-2}$ in the time scale of $1\ s$. Variations of ω_s are of the relative magnitude of 10^{-3} in the time scale of $1\ s$. First plot shows a comparison between the detected frequency, the real Sagnac frequency and the EKF corrected frequency at $5\ kHz$; in the second plot all signals have been decimated of a factor 5000 with a moving average of $1\ s$. Last plot displays the detected frequency error for $1\ h$ of simulated and identified data at $1\ Hz$.

6.6   Identification of G-PISA Parameters

The implemented identification routine has been run on the real data in order to identify G-PISA parameters. Light intensity signals have been calibrated. $I_\pm$ have been rescaled according to

$$I = P/s \quad ,$$

(6.1)

where s is the surface of the laser section, given in Eq.(3.5). The output power is in relation with the voltage acquired following

$$P = V/G_{pd}/a_{eff} \quad ,$$

(6.2)

where V is the output voltage revealed, G_{pd} is the amplifiers gain, a_{eff} is the quantum efficiency of the reveler.

For G-PISA photo diodes and amplifiers these constants are $G_{pd} = 10^9$, $a_{eff} = 0.4$. The above considerations lead to a calibration constant of $0.0167084 \, V^{-1}$.

After calibration the simulation routine has been tested on G-PISA operation of the day of 15/09/2011, the results are shown in Fig.6.10.

6.7   Frequency Estimation on a typical G-PISA day of Operations

After the identification of G-PISA parameters, the EKF frequency estimation routine has been tested. Light intensities have been calibrated and normalized to the Lamb units. The interferogram signal have been normalized and detrend to a sinusoidal signal with unit amplitude and zero offset.

Results are shown in Fig.6.11. The plot compares three different estimators of the Sagnac frequency: the numerical derivative of the EKF output x_3, the previous signal corrected by the back-scattering contribution as modeled by Eqs.(3.3) and the identification PEM method AR2 which is the standard for the estimation of the Sagnac frequency. It can be clearly seen that EKF estimation improve the performance of the frequency estimation with respect to variance, it also correct a small bias which was caused by back-scattering. The fluctuations of the red line are presumably caused by the Fabry-Peròt cavity length thermal drift, and they can be reduced by a more stable laser apparatus.
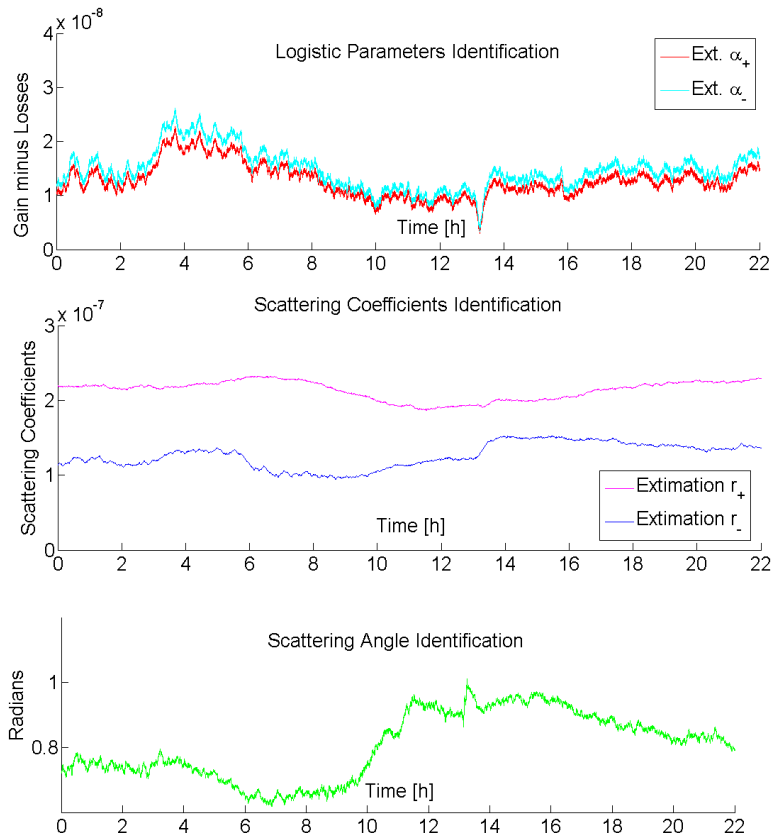
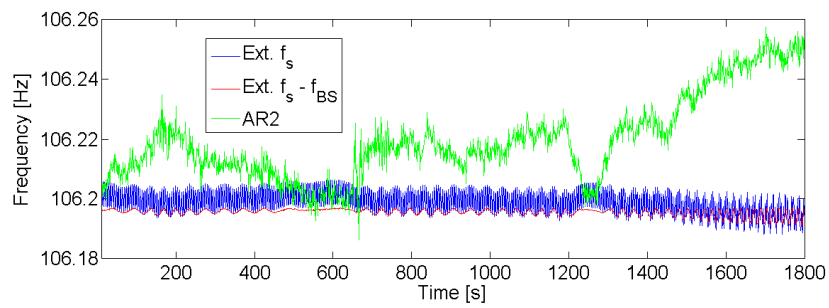Figure 6.10: Identification results for the date of 15/09/2011 (GPS = 10000000000).

Figure 6.11: Frequency estimation results for the date of 15/09/2011.

Conclusions

In this thesis we have discussed RLG as high sensitivity sensors of inertial rotation measurement. The Sagnac effect and the laser physics exploited in RLG operation have been described. A full model of the RLG dynamic has been studied, with attention to the active controls implemented for the G-PISA ring laser. We remark that the approach based on the RLG dynamical model differs from other approaches reported in the literature (e.g. standard frequency error model [9]). The study of the RLG dynamic has been completed with numerical integration methods and a simulation routines. We succeeded in implementing an identification procedure, and we also studied the effects of the approximations on the identified parameters. We implemented an EKF routine based on the RLG dynamic model and on the identified RLG parameters, and the routine was tested on simulated and experimental data, and the results discussed.

Parametric models derived by the laser physics have been proposed in high precision laser instrumentation field, since laser discovery. We think that a parametric identification approach will have best performances in the estimation of the Sagnac frequency. Our identification procedure shows a relative error on the RLG parameters $\delta\mu_\pm = 1.7 \cdot 10^{-2}$, $\delta r_\pm = 1.3 \cdot 10^{-3}$ and $\delta\varepsilon = 3.3 \cdot 10^{-3}$, and our EKF routine is able to estimate the frequency signal with an error of the order of 10^{-5} Hz.

The filtering and identification procedures discussed and implemented in this thesis can be further improved. For instance, the numerical integration method RK-4 presents an integration error that increase with time. However, further investigations can be performed on geometrical integrators and on energy conservative modifications of Runge-Kutta routines. Finally, the EKF model provided can be improved increasing the state dimension and modifying the measure model.

The work of this thesis has been carried out in collaboration with the researchers of G-PISA experiment. Some considerations on the identification and frequency estimation procedure, especially these involving loops will lead to hardware improvements in the future. For instance, the perimeter loop can be improved by a different stabilization scheme where all the four mirrors are actively controlled by mean of piezo actuators. The intensity loop can be also improved considering

the losses μ_- effect on intensities. Both loops can be optimized with optimum control and minimum variance techniques. In conclusion manufacturing and data processing fields are shown to increasingly interact as one tries to overcome the present limitations of RLG sensitivity and stability.

References

[1] D.Loukianov, R.Rodloff, H.Sorg and B.Stieler, *Optical Gyros and their applications,* RTO AGARDograph 339, Introduction, **2**.1-**2**.15 (1999).

[2] Mr. S. Leek et al, *INS/GPS technology trends,* RTO AGARDograph 339 (2011).

[3] K.U. Schreiber, J.P.R. Wells, G.E. Stedman, *Noise processes in large ring lasers,* International Journal of Modern Physics D (IJMPD), Gen. Relativ. Gravit. **40**, 935-943 (2008).

[4] J. Belfi et al., *Measuring the Virgo-area Tilt Noise with a laser Gyroscope,* Department of Physics and CNISM, University of Pisa (2011).

[5] Giorgio Picci, *Filtraggio Statistico (Wiener,Levinson,Kalman) e applicazioni,* Libreria Progetto, Padova, Italy (2007).

[6] A. Di Virgilio et al., *A laser gyroscope system to detect the gravito-magnetic effect on earth,* International Journal of Modern Physics D (IJMPD), Gen. Relativ. Gravit. **19**, 2331-2343 (2010).

[7] G E Stedman, *Ring-laser tests of fundamental physics and geophysics*, Rep. Prog. Phys. **60**, 615–688 (1997).

[8] Frederick Aronowitz, *Optical Gyros and their applications,* RTO AGAR-Dograph 339, Introduction, **3** (1999).

[9] Alexander Velikoseltsev, *The development of a sensor model for Large Ring Lasers and their application in seismic studies,* Thesis (2005).

[10] Jacopo Belfi et al., *A 1.82 m^2 ring laser gyroscope for nano-rotational motion sensing,* 16 Aug 2011, Applied Phisics B - Lasers and Optics (2011), (online version, DOI 10.1007/s00340-011-4721-y).

[11] FEMTO, *Datasheet LCA-4K-1G*, Messtechnik, GmbH Klosterstr, Berlin, Germany.

[12] Hamamatsu, *Datasheet Series S1337,* Cat. no. 0.000530609 V, 2004 Milan.

[13] Alexander A. Trusov, *Allan Variance Analysis of Random Noise Modes in Gyroscopes,* Thesis (2011).

[14] J. D. Cresser, W. H. Louisell, P. Meystre, Schleich, M. O. Scully, *Quantum noise in ring-laser gyros. Theoretical formulation of problem,* Phys. Rev. **A 25**, 4 (1982).

[15] Burr-Brown Corporation*, Photodiode monitoring with op amps* AB-075, application bullettin, printed in U.S.A. January 1995.

[16] Howard M.Taylor, Samuel Karlin, *An introduction to stocastic modeling,* Mc Graw Hill, Singapore (1998).

[17] T.V. Radina, A.S. Stankevich*, Nonreciprocity of losses and shift of the zero point in a laser gyroscope,* Optics and Spectroscopy, **95**, 956–966 (2003).

[18] Athanasios Papoulis, *Probability, Random Variables, and Stochastic Processes*, Mc Graw Hill, Singapore (1984).

[19] Frederik Aronowitz, *Lock-in and Intensitiy-Phase Interaction in the Ring Laser,* Journal of Applied Phisics, **41**, 130 (1970).

[20] Giovanni Marchesini, Giulia Prando, *Appunti di Sistemi Ecologici,* Libreria Progetto, Padova, Italy (2011).

[21] L.N. Menegozzi, W.E. Lamb Jr., *Laser Amplification of Incoherent radiation,* Physical review **A 17**, 2 (1978).

[22] Ai-Guo Xiao, *Error analysis of variable stepsize Runge-Kutta methods for a class of multiply-stiff singular perturbation problem*, BIT Numerical Mathematics **28**, 3, 678-700 (1988).

[23] William H. Press, Saul A. Teukolsky, William T. Vetterling, Brian P. Flannery, *Numerical Recipes 3rd Edition: The Art of Scientific Computing,* September, Cambridge, (2007).

[24] D. T. Pope, H. M. Wiseman and N. K. Langford, *Adaptive phase estimation is more accurate than non-adaptive phase estimation for continuous beams of light*, Phys. Rev. (A), **70**, 4 (2004).

Aknowledgements

I want to thank Prof. Alessandro Beghi, who dragged me into this adventure, and Dr. Antonello Ortolan, who showed me that a supervisor can be at the same time authoritative as well as open-minded and friendly.

I also thank the whole G-PISA team, especially Dr. Jacopo Belfi, Dr. Angela Di Virgilio, Dr. Bachir Bouhadef and Dr. Fabio Stefani, for their valuable support and for the patience they showed me for answering to my repetitive questions.

Finally, I want to thank my family, Giulia, Federico, Renata and Riccardo, for their unique and wonderful psychological support.

I thank you all!